

UNIVERSITY COLLEGE LONDON

UCL PHD UPGRADE REPORT

Qubit Coherence and Control

Author:

David F. WISE

Supervisor:

Prof. John MORTON

Submitted in partial fulfilment for the degree of **MRes Quantum Technologies**

March 14, 2018

ABSTRACT

Scientific documents often use \LaTeX for typesetting. While numerous packages and templates exist, it makes sense to create a new one. Just because.

CONTENTS

1	INTRODUCTION	1
2	THEORY	5
2.1	Electron Spin Resonance	5
2.1.1	Background Theory	5
2.1.2	Pulsed Electron Spin Resonance and Qubits	6
2.2	Donor States in Silicon	7
2.2.1	The Hyperfine interaction	7
2.2.2	Spin Transitions	8
2.2.3	Relaxation Processes	10
2.2.4	Summary	11
3	LITERATURE REVIEW	13
3.1	Mechanisms of Relaxation and Decoherence	13
3.1.1	Relaxation	13
3.1.2	Decoherence	14
3.2	Illumination and Decoherence	16
3.2.1	Free Carriers and Decoherence	16
3.2.2	Heating and Decoherence	18
3.3	The Stark Shift	20
3.3.1	Introduction	20
3.3.2	Theory	20
3.3.3	Stark Shift Measurement Techniques	23
3.3.4	Stark Shift Experimental Results	25
3.3.5	The Nuclear Spin Bath in Natural Silicon	26
3.4	Summary	26
4	EXPERIMENTAL METHODS	27
4.1	Equipment	27
4.1.1	Cryogenic and Microwave Instrumentation	27
4.1.2	Laser	28
4.2	Pulse Sequences	28
4.2.1	ESR Pulse Sequences	28
4.2.2	Nuclear Pulse Sequences	30
4.3	Experimental Set-ups	32
4.3.1	Laser Experiments	32
4.3.2	Stark Shift Experiments	33

Contents

5	RESULTS	35
5.1	Illumination Induced Decoherence	35
5.1.1	Initial Measurements	35
5.1.2	Bi-Exponential Inversion Recovery	35
5.1.3	High Power Wavelength Comparison	36
5.1.4	Temperature Comparison	41
5.1.5	Heating as a Mechanism of Relaxation	42
5.2	Stark Shift Experiments	45
5.2.1	Stark Shift on Selenium Donors	45
5.2.2	Stark Shift on ^{29}Si Nuclei	46

LIST OF FIGURES

2.1	Free electron level splitting	5
2.2	Hahn echo sequence	7
2.3	Bloch Sphere	8
2.4	Phosphorus energy levels and transitions	9
3.1	Decoherence mechanisms in silicon	17
3.2	T_1 dependence on photon energy	19
3.3	Electron wavefunction Stark shift	20
3.4	Silicon band structure	21
3.5	Phosphorus field sweep	24
3.6	Stark shift sequence	24
3.7	Wolfowicz <i>et al</i> Stark measurements	25
4.1	Rabi Sequence	28
4.2	Inversion recovery and T_2 pulse sequences	29
4.3	CPMG pulse sequence	30
4.4	Davies ENDOR sequence	31
4.5	Nuclear echo pulse sequence	32
4.6	Full coherence transfer	32
5.1	T_1 and T_2 decays	36
5.2	Inversion recovery under laser illumination	37
5.3	Bi-exponential relaxation decay constants	38
5.4	Relaxation comparison at 8k and 1058nm, 1070nm, and 1080nm illumination	39
5.5	T_1 vs T_2 for 1058nm and 1070nm	40
5.6	Low power T_1 and T_2 comparison	40
5.7	T_1 temperature comparison	42
5.8	Simulated T_1 under heating	44
5.9	Stark shift in Bismuth	45

1 INTRODUCTION

*At midnight all the agents and
superhuman crew come out and round
up everyone that knows more than they
do*

Quantum computing has been an active field of research since the concept was first suggested by Richard Feynman in the early 1980s [14]. Originally proposed as an efficient method for simulating chemical processes (something that traditional computers find extremely taxing) the discovery of several algorithms offering significant speed increases over classical computers has further fuelled research [38, 39]. Strong initial scepticism abounded regarding the potential for quantum computers to exist in the real world, primarily due to the concerns that error correction with such a complex device would be impossible [32]. This pessimism gave way with the identification of an error threshold for quantum computation. Given an error rate below a critical threshold it was possible to perform an arbitrarily long computation with negligible possibility of significant error [1, 37]. Following these discoveries serious attention has been given to the development of error correcting codes that might be implemented to allow a physical quantum computer to be *fault tolerant*.

Gottesman identified the class of error correcting codes known as *stabilizer codes*, where codes are defined by the group of logical operators that leave the code unchanged [18]. This class of quantum error correcting codes have become the dominant form in theoretical research. Of these one in particular has become the focus of much of the ongoing research of quantum computing, *the surface code*, developed by Bravyi and Kitaev [6]. Although other quantum error correcting codes (such as colour codes [44]) exist, the surface code has become the focus for experimental implementations. This is due mainly to the relatively high error threshold that it is able to tolerate, $\sim 0.5\%$, and the simple architecture of a planar grid of qubits.

In recent years there has been rapid progress in the development of physical qubits. Groups in both the academic and private sectors have shown small numbers of qubits functioning with error rates above the fault tolerant threshold [4, 33]. The successful recent approaches

have tended to focus on superconducting circuits to produce their qubits. Whilst these have proved excellent for the small numbers of qubits currently in use, it is likely that they will present significant additional challenges when scaling to numbers sufficient for useful, fault-tolerant quantum computation. With the numbers required likely to be close to 100×10^6 and the current size of these qubits close to 1mm^2 , it will likely be impossible to use these qubits in their current form in a fault-tolerant quantum computer.

Although there are many alternative systems that could provide a qubit, this paper will focus on the use of the spins of nuclei and electrons bound to donors in semiconductors, particularly silicon. A seminal paper by Kane [20] stimulated much of the research interest in this field. He proposed using the spin of phosphorus nuclei in silicon as qubits with the ability to mediate interactions between neighbouring donor nuclei using the interaction between the electrons bound to each. These types of qubit are attractive due to their exceptionally long coherence times, the time that the qubit reliably stores quantum information for. A long coherence time relative to qubit gate times is essential, as this determines the error rate of the qubits. Coherence times as long as several seconds have been reported for donor spin qubits in silicon, whilst gate times can be as low as several nanoseconds [48]. Despite these advantages, development of these types of qubits for quantum computers has lagged behind the superconducting and ion trap versions [2]. This is due to the difficulty of isolating and addressing single donors in a silicon lattice. Kane's proposal required sub nano-metre precision in qubit placement to facilitate inter-qubit interactions. Even if this precision were achieved there remains the issue of how the requisite control circuitry could be integrated into such a dense design. This has led to the development of more modern proposals to both overcome these difficulties and also to implement surface code based error correction.

One such proposal is from O’Gormann et al [29]. This proposal takes a similar approach to Kane, with qubits being donor spins in a silicon lattice. Where it differs significantly is in its use of two lattices of qubits. One of these is for the storage of data, whilst the other performs measurements on these data qubits. This measurement stage is placed above the data stage and held close, within 40nm, and moved in a repeating cycle over the data qubits. This allows each measurement qubit to perform \hat{X} or \hat{Z} measurement on groups of four data qubits, the stabilizer measurements that make up the fundamental units of surface code. This architecture allows for data qubits to be placed much farther apart - since no direct interaction between them is required. Several key research questions remain:

1. What donor species should be used for both types of qubit?
2. How are the measurement qubits to be read out?

3. How are the qubits to be controlled?

Whilst donors in silicon make excellent choices for the data qubits due to the properties stated above, a different qubit species is required for the measurement qubits to avoid an unwanted exchange interaction between the two lattices. Optical qubit readout is suggested in the proposal by O’Gormann et al and is a well studied means of reading the state of spin qubits, particularly in nitrogen-vacancy (NV) centres in diamond [21]. A concern with optical readout is the impact that illumination can have on the coherence times of donors in silicon. Silicon has a band gap energy equivalent to approximately 1058nm or photon energy of 1.17eV. Illumination at shorter wavelengths than this will create free electrons in the silicon conduction band. These can scatter off the electrons bound to donors, causing them to relax and shortening the T_1 time of the qubits as a whole [Ross2017]. NV centres are read out at between 500nm and 600nm, illumination that would reduce data qubit coherence times and increase the qubit error rate. Alternative optically addressed spin qubits at higher wavelengths exist, such as the di-vacancy centre in silicon carbide [9], but a vital question is what wavelengths can be used for read-out without compromising data qubit coherence times. This report addresses this question by examining the effect of various laser wavelengths close to the silicon band gap on the coherence times of electrons bound to phosphorus donors in silicon.

Another key question presented by the O’Gormann proposal is how to control the data qubits. The frequencies traditionally used for electron spin resonance are between 8GHz and 10GHz. Electromagnetic radiation at these frequencies require large coaxial cables and cavities for transmission. This makes it almost impossible to individually address qubits using microwaves. Instead the solution proposed by Kane is to use global microwave pulses, addressing all qubits at once. To selectively control qubits the DC Stark shift can be employed - DC electric fields can be used to shift the electron spin transition frequency meaning that a global microwave field will not effect them. Unlike RF radiation, DC signals are easily multiplexed and the commercial electronics industry has achieved fabrication precision well within that required by the O’Gormann proposal. In addition to the potential control benefits provided by the Stark shift, it can bring problems. Inhomogeneous electric fields near spin qubits would alter the energy of their transition, potentially leading to decoherence. It is also beneficial, therefore, to identify systems that only experience a small Stark shift, as this would render them much more resistant to electric field noise and make them potentially ideal data qubits. One such system is explored in this report, the unpaired electron bound to a selenium⁺ donor in silicon. Among these is the hyperfine interaction between the donor electron and the silicon-29 nuclei present in natural silicon. The nuclear bath has been iden-

1 Introduction

tified as a potential quantum register and the ability to tune the interaction between data qubits and memory could be of use.

2 THEORY

2.1 ELECTRON SPIN RESONANCE

2.1.1 BACKGROUND THEORY

Electron spin resonance (EPR) functions by detecting the energy difference between the spin states of an electron. Normally degenerate, the presence of a magnetic field separates the two spin states parallel to it in energy - known as the Zeeman splitting [13]. The spin state parallel to the magnetic field has a lower energy whilst the anti-parallel state has a higher energy. These are described as the up, $|\uparrow\rangle$, and down, $|\downarrow\rangle$, spin states. For an electron in free space the energy difference is given by:

$$\Delta E = g_e \mu_b B, \quad (2.1)$$

where g_e is the free electron g-factor, μ_b is the Bohr magneton and B is the magnetic field strength. This results in an energy splitting as seen in figure 2.1.

In practice this energy splitting can be detected using continuous wave EPR. Transitions between the spin states will be driven by incident electromagnetic radiation of photon energy equal to the energy gap (i.e $h\nu = g_e \mu_b B$). The presence of an EPR transition in a sample can be detected either by applying a constant magnetic field and sweeping EM frequency

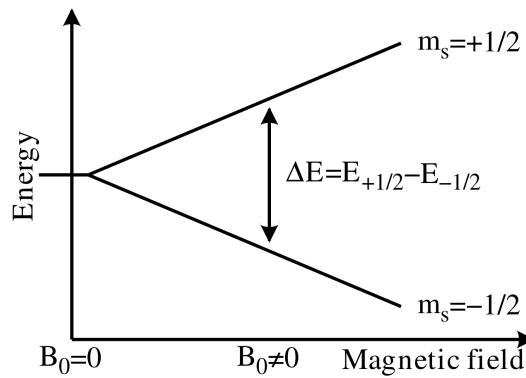


Figure 2.1: Spin state energy splitting for a free electron in a magnetic field.

incident on that sample or vice versa. In practice, it is the latter that is used for experimental simplicity. Measuring reflection of radiation from the sample whilst sweeping magnetic field will reveal a drop in reflection at the transition field - when photons are absorbed by spins moving from the lower to higher energy state.

2.1.2 PULSED ELECTRON SPIN RESONANCE AND QUBITS

The description above details continuous wave (CW) ESR, a technique that has proven invaluable for studying the electronic structure of materials. Another ESR has proven more popular for the manipulation of spins for use of qubits: pulsed ESR. This uses short bursts of microwave radiation, on resonance with the spin transition, to control spin states and allows the spin to function as a qubit. This control is achieved by placing the spins at the centre of a cavity which produces a magnetic field when a pulse is applied. This magnetic field causes precession which can be used to rotate the spins. Pulses are described in terms of a rotation angle, with a π pulse taking the ensemble of spins from the down to up state or vice versa. A $\pi/2$ pulse takes the spins into the plane normal to the magnetic field, termed the $x-y$ plane. This causes the spins to precess in the static magnetic field at the Larmor frequency given by:

$$\omega = \frac{eg}{2m} B_0 \quad (2.2)$$

HAHN ECHO AND DETECTION

In pulsed ESR the spins are detected via the electromagnetic radiation they emit when precessing in a magnetic field. This radiation is of the same frequency as the resonant control radiation (easily shown using equations 2.1 and 2.2). This emitted radiation can be demodulated with the control radiation giving a DC signal. In a perfectly homogeneous magnetic field all spins would precess at the same rate giving a constant DC signal. In reality however, all spins will precess at slightly different rates due to small, static differences in the magnetic field each experiences. So, following a $\pi/2$ pulse, the signal from the spins will rapidly decay as the ensemble of spins lose phase coherence. A technique, known as a spin or Hahn echo, to reverse this loss of phase was developed by Erwin Hahn in 1950 [19]. This follows a $\pi/2$ pulse with a π pulse after a set time interval, T . Static magnetic field differences now act to reverse the loss of phase coherence. This results in a brief re-phasing of the spins following another interval T , detected as a rise and fall of a DC signal or and ‘Echo’. A cartoon of this sequence is shown in figure 2.2.

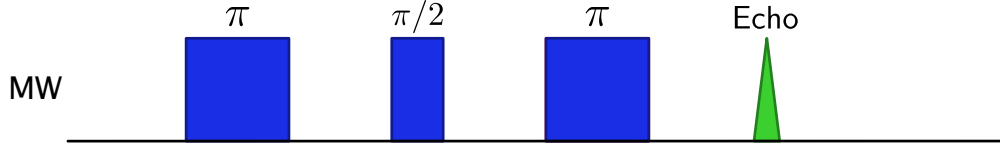


Figure 2.2: Cartoon showing a Hahn echo pulse sequence. A $\frac{\pi}{2}$ pulse causes the spins to precess in the $x - y$ plane. Loss of phase coherence is reversed via a π pulse following time interval T and a signal is detected following another interval of T .

THE BLOCH SPHERE

The control pulses produce a magnetic field that rotates at the same rate as the spins, meaning a fixed coordinate system can be defined. The rotation axis of the control pulses can be changed by varying their phase, for example to a pulse of 0 phase is defined as a rotation about the x axis whilst a pulse of $\pi/2$ phase is a rotation about the y . This allows control of the direction of the spin vector in 3-D space, with the z -axis defined by the static magnetic field. A qubit, the basic unit of a quantum computer, can be described as a point within a unit sphere, known as a Bloch sphere and shown in figure 2.3 [27]. Clearly then, a single spin is an archetypal qubit: its eigenstates of $|\uparrow\rangle$ and $|\downarrow\rangle$ form the poles of the Bloch sphere. Microwave pulses of defined duration and phase enable the creation of an arbitrary linear superposition that allows the initialisation of any state on the surface of the Bloch sphere. In the case of ESR, however, a huge number (10^{10}) of spins is being addressed. Although this means that they do not represent a true qubit, measurements of ensemble properties give great insight into the behaviour of single spins. It is therefore prudent to establish the anticipated behaviour of the various potential spin qubit candidates using the comparatively simple experimental techniques of ESR before making the challenging step to single spin control and measurement.

2.2 DONOR STATES IN SILICON

2.2.1 THE HYPERFINE INTERACTION

Discussion so far has focussed on single electrons in a magnetic field. The spins discussed in this thesis will be those of the electrons and nuclei of donors in silicon. For these spin states the situation is a little more complicated than the case of a free electron. For all the donors discussed here, there is a nuclear as well as electron spin. This introduces first an additional term in the Hamiltonian of the system due to the nuclear spin's Zeeman interaction with the magnetic field. On top of the separate Zeeman interactions there is an additional interaction

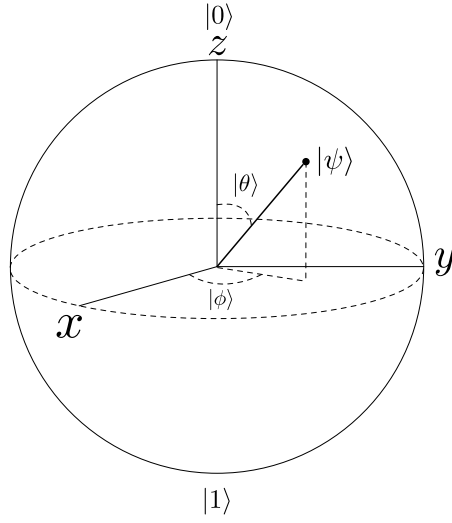


Figure 2.3: Diagram of the Bloch sphere - the most common representation of a qubit. The poles of the sphere at $\pm z$ represent the $|0\rangle$ and $|1\rangle$ or $|\uparrow\rangle$ and $|\downarrow\rangle$ states. Any point on the surface of the sphere represents some linear superposition of these two states. The state vector of any point is given by: $|\psi\rangle = \cos \theta/2 |0\rangle + e^{i\phi} \sin \theta/2 |1\rangle$

between the nucleus and the electron, known as the hyperfine interaction. This term is due to the magnetic field of the electron interacting with the magnetic dipole moment of the nucleus. This strength of this interaction is proportional to the overlap between the electron and nuclear wavefunctions. The result of this is that it is preferential energetically for the electron and nuclear spins to be anti-aligned. A further term in the Hamiltonian is due to the nuclear quadrupole but this effect is small enough to be neglected in this treatment. These effects leave a Hamiltonian of the following form:

$$\hat{H} = \mu_b g_e B_0 \hat{S}_z + \mu_n g_n B_0 \hat{I}_z + A \hat{S} \cdot \hat{I}, \quad (2.3)$$

where μ_b & μ_n are the Bohr and nuclear magnetons, g_e & g_n are the electron and nuclear g-factors, \hat{S} & \hat{I} are the electron and nuclear spin operators, and A is the hyperfine interaction term. In general they hyperfine term is a tensor but due to the isotropic nature of silicon can be represented as a scalar here.

2.2.2 SPIN TRANSITIONS

The electron spin is restricted to be $\pm \frac{1}{2}$, but the nuclear spin can take a much greater range of values. The nuclear spin of a phosphorus donor in silicon is $\pm \frac{1}{2}$, by contrast for a bismuth

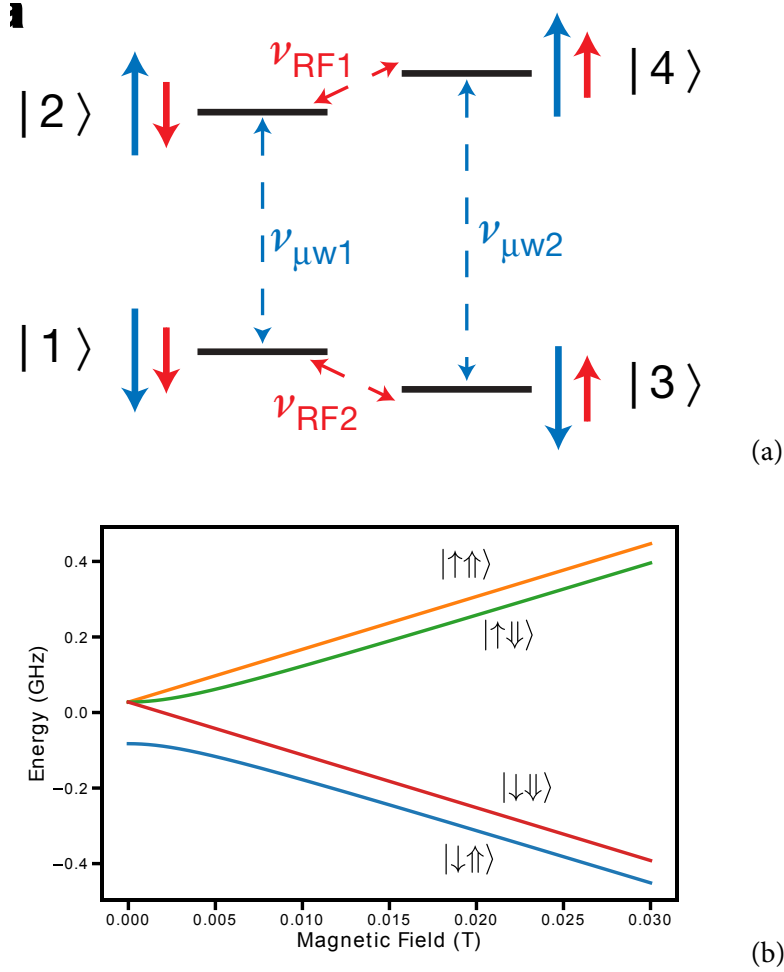


Figure 2.4: Cartoon in a shows the relative energy levels for the different spin states of phosphorus in a high field environment. Note that in this case the electron Zeeman interaction dominates the hyperfine term which dominates the nuclear Zeeman term. b shows the simulated energies for each of the four possible states of the system.

spin it can take the values $-\frac{9}{2}, -\frac{7}{2}, \dots, \frac{7}{2}, \frac{9}{2}$. In the simple case of phosphorus this results in the four energy levels seen in figure 2.4.

For the more complex case of bismuth, instead of 4 possible energy levels there are 20. Not all transitions are possible - spins are changed by the absorption or emission of a photon, leaving only transitions where the total spin changes by ± 1 as allowed. This means that only nuclear or electron spin can be flipped at once, not both. It should be clear that the transitions that involve an electron spin flip (e.g. $|\uparrow\uparrow\rangle \rightarrow |\downarrow\uparrow\rangle$) are significantly higher in energy than those involving a nuclear spin flip (e.g. $|\uparrow\uparrow\rangle \rightarrow |\uparrow\downarrow\rangle$). At typical experimental magnetic fields (≈ 0.3 Tesla), the nuclear transitions are at frequencies of 10s of MHz, whilst

the electron transitions are at ≈ 9.7 GHz. In addition to their different energies electron and nuclear transitions have different strengths or Rabi frequencies. The electron spin transition is much stronger and occurs on the order of nanoseconds at typical pulse powers, with the nuclear transition being on the order of microseconds.

2.2.3 RELAXATION PROCESSES

For spins in silicon, three main relaxation or decoherence processes occur, causing the loss of information.

Dephasing

The first of these was briefly discussed above - dephasing - the time scale for the process is termed T_2^* . This is the process by which an ensemble of spins loses phase coherence due to each spin experiencing a different static magnetic field. As was described above, this loss of information can be reversed by a Hahn echo sequence.

Relaxation

The second process is known as relaxation and its time scale is termed T_1 . A spin ensemble at a given temperature and magnetic field will have a Boltzmann distributed population across the available spin states defined by the magnetic field axis (i.e. across the eigenstates of the \hat{Z} operator). The difference between higher and lower energy states is known as the polarisation of the ensemble. If this polarisation is reversed by a π pulse, then on a time scale T_1 it will relax back to thermal equilibrium. As this process almost always involves interaction with the silicon crystal lattice it is also termed *spin-lattice* relaxation. This process is strongly correlated with temperature and exact mechanisms will be discussed in the literature review section.

Decoherence

The third process, decoherence, occurs on the time scale T_2 . This is similar to the dephasing process described above but is irreversible. Irreversible phase differences are caused by inhomogeneous and *time dependent* magnetic fields. Additional phase acquired due to a time varying magnetic field will not be reversed by a Hahn echo sequence as the field will act differently on the spin in the second half of the sequence.

2.2.4 SUMMARY

The theory discussed above gives a background to the topics that will be discussed in detail during the literature review section of this report.

3 LITERATURE REVIEW

Having introduced the background theory to the work discussed in this report, I turn to a more detailed examination of the literature surrounding this work. I begin with the various relaxation and decoherence processes for spins bound to donors in silicon. First discussing the mechanisms by which these processes occur I shall then move on to the effect of illumination on these mechanisms. Following this I shall move on to the stark shift of donor spins in silicon, including a brief introduction to the principle before an examination of previous work performed to characterise this effect in the various species of donor in silicon.

3.1 MECHANISMS OF RELAXATION AND DECOHERENCE

The concept of T_1 , T_2 and T_2^* time was introduced in section 2.2.3 as the characteristic relaxation, decoherence and dephasing respectively. I shall now focus on the established mechanisms by which these occur, looking mainly at relaxation and decoherence as these represent a permanent loss of information.

3.1.1 RELAXATION

The relaxation time, T_1 , determines the rate at which the polarisation of an ensemble of spins returns to Boltzmann equilibrium after being disturbed. The first method of relaxation that should be considered is spontaneous emission: the emission of a photon into free space as the spin relaxes from excited to ground state. For a magnetic dipole this rate is slow in normal circumstances - thousands of seconds or more [3, 35]. Given that above millikelvin temperatures the rate of transverse relaxation for donor spins in silicon is significantly greater than this it can be neglected as a dominant mechanism.

Spin-lattice relaxation occurs instead via the interaction with of the spin system with vibrations in the silicon lattice - phonons. There are three different phonon-mediated processes that affect the relaxation rate of spin systems with transition frequency ω_s , all of which are well described in a 1961 paper by Orbach [30, 43].

Direct Process

The first of these is a **direct process**, whereby a single phonon with frequency equal to that of the spin transition (as given by equation 2.3) is emitted into the lattice. This rate ($\propto 1/T_1$) is proportional to the phonon density at ω_s and varies with spin transition frequency and temperature as: $\omega_s^4 T^{-1}$.

Raman Process

Whilst this rate dominates at lower temperatures, $< 10\text{k}$, at temperatures with $k_B T \gg \hbar\omega_s$, a two phonon Raman transition becomes more efficient. As the maximum phonon density is at much higher frequencies than ω_s , the spin first absorbs a phonon at ω_{max} before emitting a phonon with $\omega = \omega_{\text{max}} + \omega_s$. This corresponds to the spin transitioning to a virtual energy level before rapidly transitioning back to the spin ground state. For non-integer spin systems the rate due to this effect scales with temperature as: T^7 .

Orbach Process

The Raman process involves a virtual energy level so is an inherently off-resonant effect. It is possible for the spin to transition to an actual excited state during the two phonon process. This is known as an Orbach process and is more efficient than either process above. It scales with temperature as: $\exp(-\Delta E/K_B T) - 1$.

3.1.2 DECOHERENCE

At high temperatures the spin-lattice relaxation rate tends to be the dominant process for spins in silicon. However, at temperatures below $\approx 10\text{k}$ other factors become limiting. In particular the decoherence or T_2 time becomes important. This is the process by which the spins lose phase coherence irreversibly. There are several mechanisms that contribute to T_2 , detailed here.

Spectral Diffusion

The first of these is spectral diffusion and its impact is largely dependent on the sample used. In natural silicon samples there is a relatively high concentration of Spin- $\frac{1}{2}$ ^{29}Si nuclear spins (4.7%). Due to the large extent of the donor electron wavefunction, it is highly probable that a given donor will experience a hyperfine interaction with one or more of these nuclei. Although the large difference between the electron and nuclear gyromagnetic ratios prevents a state exchange or 'flip-flop' interaction, nearby pairs of ^{29}Si nuclei do have this interaction. The rate of exchange is slow, ($\approx 100\text{Hz}$) and will cause a change in the hyperfine interaction with any nearby donor electrons. This will cause the acquisition of phase differences between electrons over time. As these changes are time dependent they are *not* refocused by a Hahn

echo sequence [46]. In purified silicon samples this effect is reduced to the point that it is no longer the limiting factor in spin coherence.

Instantaneous Diffusion

In the first experiments on spin coherence times on purified silicon, the increase in coherence time was found to be on the order 2 fold [17]. The reason behind this limited increase was the high donor concentrations, leading to interaction between donors. Spins close enough to interact with one another will experience slightly different magnetic fields and the random nature of donor distribution leads to this effect being inhomogeneous. Once again, this will not be reversed by a Hahn echo sequence as two donors interacting with one another will both be flipped, meaning that the phase acquisition is unchanged. This effect is dependent on the concentration of donors in a sample according to:

$$\frac{1}{T_2^{\text{ID}}} = C(2\pi\gamma_e)^2 \frac{\pi}{9\sqrt{3}} \mu_0 \hbar, \quad (3.1)$$

where C is the donor concentration.

At concentrations useful for ESR techniques and at sufficiently low temperatures instantaneous diffusion will be a limiting factor in spin coherence times in almost all cases. One technique employed by Tyryshkin *et al*, open to ensemble based approaches such as ESR but not to single qubit control, is to use refocussing pulses of angle $< \pi$ in the Hahn echo sequence [41]. This effectively refocuses fewer spins during the Hahn echo sequence. This reduces the signal but increases T_2 time as the effect of instantaneous diffusion is suppressed by addressed spins being on average much further apart. At this point three further effects become limiting:

- *Direct T_1 Flips*: only relevant at higher temperatures when T_1 is close to the intrinsic T_2 , $> 10\text{k}$. This is the process of a single donor flipping to its ground state, thereby destroying its coherence.
- *Spectral Diffusion from donors*: the limiting factor at low temperatures $< 4\text{k}$, this process is similar to the spectral diffusion for ^{29}Si spins. Nearby pairs of donors undergo spin exchange, causing any other nearby donors to experience a phase shift as their hyperfine coupling changes.
- *T_1 of Neighbouring Donors*: this process is important at intermediate temperatures, between 4k and 10k . At these temperatures direct T_1 flips are yet to dominate but T_1 flips of neighbouring donors can affect the magnetic field experienced by a central donor. This effect is known as T_1 -type spectral diffusion. This process was identified by Tyryshkin *et al* as producing lower than expected T_2 times when T_1 ap-

peared to no longer be a limiting factor [41]. The decoherence rate as a function of T_1 induced spectral diffusion has a characteristic, stretched exponential of the form $\exp(-(2\tau/T_{SD})^2)$, with $T_2^{SD} = \sqrt{T_1}$.

The five key contributors to decoherence are shown in figure 3.1. The key contributors to decoherence times are then:

- *Temperature*: when T_1 is sufficiently short at high temperatures the T_1 of the donors will restrict T_2 . At intermediate temperatures T_1 flips of neighbouring donors induces spectral diffusion, reducing T_2 .
- *Sample Purity*: the concentration of ^{29}Si spins in the silicon has a significant impact on T_2 due to spectral diffusion via nuclear spin flip-flop.
- *Donor Concentration*: the concentration of donors increases the rate of instantaneous diffusion, indirect flip-flop, direct flip-flop and T_1 type spectral diffusion.

With the mechanisms of decoherence addressed, we now turn to examine the effect of illumination on donor relaxation and coherence rates.

3.2 ILLUMINATION AND DECOHERENCE

3.2.1 FREE CARRIERS AND DECOHERENCE

The discussion above centred on the typical factors that affect coherence and relaxation times: temperature, donor concentration and silicon purity. One of the key questions addressed in this report is the impact of another factor on relaxation times: illumination. Feher and Gere were among the first to examine this impact in their 1959 paper [15], analysed using CW ESR of phosphorus donors in silicon. The key question that they examined is the impact of illumination wavelength on relaxation time, the results of which can be seen in figure 3.2. The important result here is the sharp increase in relaxation rate as the photon energies exceed that of the silicon band gap, $\approx 1.12\text{eV}$. As this energy is exceeded by the photons, free carriers are created in the silicon conduction band as electrons are promoted from the valence band. These free carriers can scatter off the electrons bound to the phosphorus donors, causing them to relax via a state exchange. Feher and Gere postulate two possible processes that could cause this relaxation: the first is direct scattering of a donor electron by a free electron, whilst the second is a two stage process. They identify the second of these as dominant, due in the main to the low number of free electrons relative to donors in their experiments -

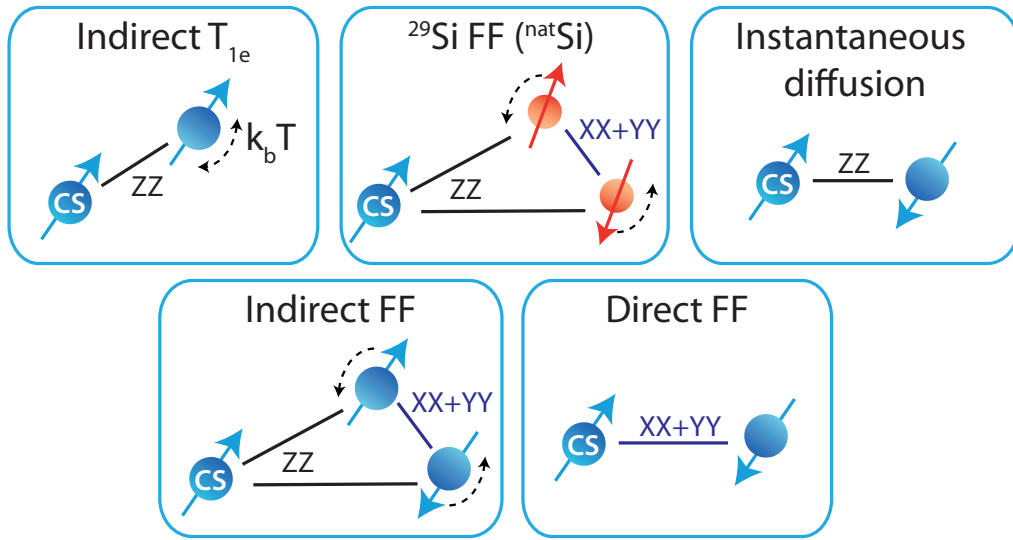


Figure 3.1: Cartoon showing the five key types of decoherence mechanisms for donor electrons in silicon. Indirect T_1 is the relaxation of a neighbouring donor modulating the magnetic field at a central donor. Flip-flops of ^{29}Si nuclear pairs modulating the magnetic field at the donor. Instantaneous diffusion is the inhomogeneous phase acquisition of donors due to different inter-donor spacings. Indirect flip-flop mechanism is similar to that involving ^{29}Si nuclei but with pairs of donors. Direct flip-flop is state exchange between a central donor and a neighbour. Figure is taken from [46].

3 Literature Review

5×10^6 vs 7×10^{15} - with each interaction requiring the subsequent relaxation of the conduction electron to the lattice. The double spin exchange process does not involve the free electron changing spin, instead both the nuclear spin of the donor and the electron bound to it change spin state. This removes the requirement that the conduction electron subsequently relax to the valence band, significantly increasing the rate of the process.

The work done by Feher and Gere was performed using only CW ESR, because of this their work addresses only the impact of laser illumination on T_1 . The key timescale for quantum computing is the coherence time, T_2 , which must be examined using pulsed ESR. Whilst T_2 time will ultimately be limited by T_1 a concern is that free carriers in the silicon conduction band will have an impact beyond this. It seems obvious that the presence of these free carriers could alter the magnetic environment of the donors in a time-dependent and inhomogeneous fashion, potentially having a drastic impact on the coherence time of donors. Examining the impact of illumination on decoherence times will be an important goal of this report.

FREE CARRIER LIFETIMES

One question that is of importance is the time that free carriers will persist for following a laser pulse, as this will determine how long their effects influence relaxation and coherence times.

3.2.2 HEATING AND DECOHERENCE

A potential factor not addressed by Feher and Gere is the potential impact that heating could have on relaxation and by extension coherence times. Although the number of free carriers produced by laser illumination will be significantly reduced as photon energies drop below the band gap, it is possible that heating could still have a significant impact. Of particular note is the reduced heat capacity of silicon at low temperatures. At room temperature heat capacity (C_p^o) is $19.1 \text{ J.mol}^{-1}\text{K}^{-1}$, but at cryogenic temperatures this is reduced by several orders of magnitude to approximately $0.004 \text{ J.mol}^{-1}\text{K}^{-1}$ at 8k [12, 28]. Clearly then the potential impact of infra-red illumination is obvious - only a small conversion of incident photons to phonons in the lattice could potentially have a significant impact on the relaxation rates for donor spins. Exploring this potential impact will be a central goal of this report.

Having looked at some of the literature surrounding the questions of relaxation and decoherence of donors in silicon, I now move on to the stark shift of donors in silicon.

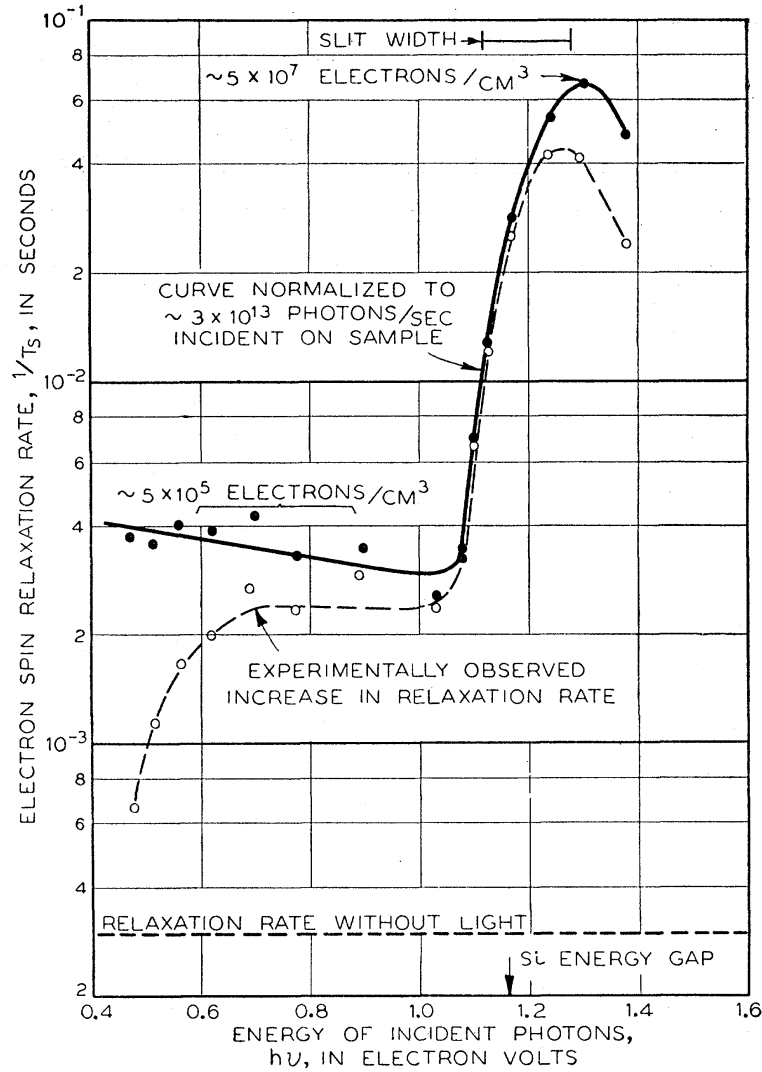


Figure 3.2: Graph from [15] showing the measured dependence of relaxation time on photon energy. Notable is the sharp increase in relaxation rate for photon energies in excess of 1.10eV. The main cause of this is that this is the energy of the photon band gap, meaning that free electrons are created in the silicon conduction band. These free electrons can then scatter off the electrons bound to donors in silicon, causing them to relax.

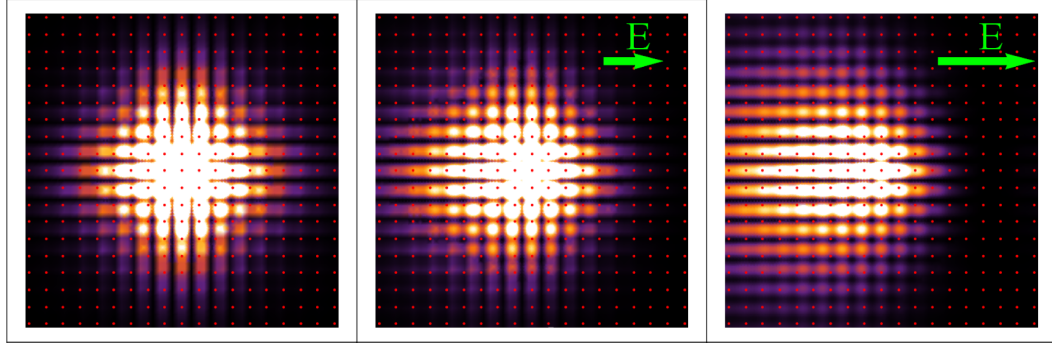


Figure 3.3: Simulation showing the density of the electron wavefunction around a donor atom. Red dots represent lattice sites. As an electric field is applied the electron wavefunction is pulled off the central site, changing the strength of its interaction with the donor nucleus and therefore its hyperfine coupling. This shifts the frequency of the electron's spin transition and its precession rate in the magnetic field. Figure reproduced from [31].

3.3 THE STARK SHIFT

3.3.1 INTRODUCTION

The Stark shift, at its simplest, is the modulation of the hyperfine coupling between electron and nuclear spins via electric fields. The Stark shift was employed in Kane's original proposal as a means to control which qubits interact with an applied control pulse [20]. As well as the potential application for control of donor spins, the Stark shift presents a problem in the potential for electric field noise to cause decoherence of donor spins. This impact may become particularly important for single donors close to electrical contacts where distances are short and so fields high. Clearly then an understanding of the stark shift and its impact on donors is useful both from control and decoherence perspectives.

An intuitive understanding of the stark shift is easily grasped: the electron's wavefunction extends over space and is concentrated at the donor nucleus. This concentration determines the hyperfine coupling of the spin to the donor. An electric field changes this wavefunction, effectively pulling it off the nucleus and changing the hyperfine coupling, as seen in figure 3.3. This in turn changes the energy difference between the two spin states of the electron and modulates its precession frequency in a static magnetic field.

3.3.2 THEORY

A technical description of the Stark shift in most cases employs effective mass theory and here I follow the approach taken by Pica *et al* [31]. This treats the donor system as if it were a hydrogen atom with a different mass embedded in a silicon lattice as opposed to a vacuum.

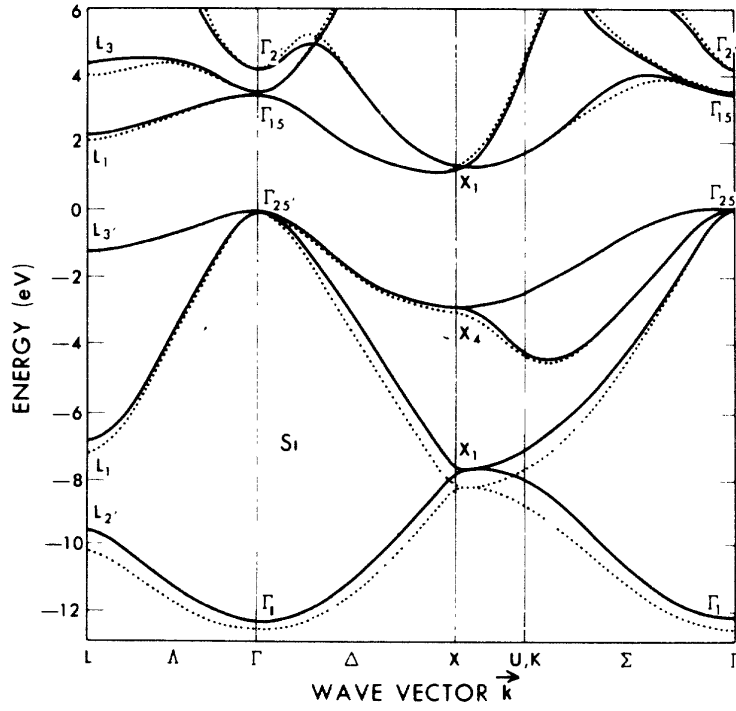


Figure 3.4: Figure from [8], showing the band structure of silicon. The top of the valence band is at Γ , the centre of the Brillouin zone, whilst the minimum of the conduction band is at X , towards the edge of the zone.

This is done by replacing the electron's vacuum mass with its effective mass in the silicon and modifying the vacuum permittivity with the dielectric constant of silicon [46]. The conduction band of silicon has 6 minima - usually termed 'valleys' - situated in the $\pm x, \pm y, \pm z$ directions and close to the edge of the Brillouin zone, as seen in figure 3.4.

The approach of effective mass theory is to decompose the electron wavefunction into six along these conduction band valleys, giving the equation:

$$\psi(r) = \sum_{i=1}^6 \alpha_i \phi_i(r) F_i(r), \quad (3.2)$$

here $\phi_i(r) = u_i e^{i\mathbf{k}_i \cdot \mathbf{r}}$, the Bloch wavefunction such that $u_i(r)$ has the periodicity of the lattice and $\mathbf{k}_i = k_0 \mathbf{i}$ with k_0 the momentum value at the valley minimum. In the electron ground state these valleys are six-fold degenerate, giving the singlet state [40]:

$$\text{Singlet } (1sA_1) \left\{ \alpha_g = \frac{1}{\sqrt{6}} (1, 1, 1, 1, 1, 1) \right. \quad (3.3)$$

This ground state is the only state with a component of the electron wavefunction at the nucleus and therefore the only one that experiences a hyperfine coupling. The excited states are as follows:

$$\text{Doublet } (1sE) \begin{cases} \alpha_r = \frac{1}{\sqrt{12}}(-1, -1, -1, -1, 2, 2) \\ \alpha_s = \frac{1}{2}(1, 1, -1, -1, 0, 0) \end{cases} \quad (3.4)$$

$$\text{Triplet } (1sT_2) \begin{cases} \alpha_x = \frac{1}{\sqrt{2}}(1, -1, 0, 0, 0, 0) \\ \alpha_y = \frac{1}{\sqrt{2}}(0, 0, 1, -1, 0, 0) \\ \alpha_z = \frac{1}{\sqrt{12}}(0, 0, 0, 0, 1, -1) \end{cases} \quad (3.5)$$

When an electric field is applied the symmetry of the valleys is broken leading to the mixing of the various states. The states interact via the electric dipole moment $e\mathbf{E} \cdot \mathbf{r}$, allowing estimation of the impact via perturbation theory. The first order perturbation to the singlet state, $\int \langle \psi_g(r) | e\mathbf{E} \cdot \mathbf{r} | \psi_g(r) \rangle d\mathbf{r}$ is zero by symmetry [31]. The second order perturbation, given by $\sum_{i \neq g} \int \frac{|\langle \psi_g(r) | e\mathbf{E} \cdot \mathbf{r} | \psi_i(r) \rangle|^2}{E_g - E_i} d\mathbf{r}$ is non-zero however, giving a to the ground state eigenfunction of:

$$|\psi_g(r)\rangle \longrightarrow |\psi_g(r)\rangle \left(1 + \frac{1}{2}\eta_A E^2\right) + \dots \quad (3.6)$$

The strength of the hyperfine interaction, A , is given by the probability density of the electron wavefunction at the nucleus: $|\psi_g(r=0)\rangle^2$. Thus the change in the hyperfine is given by:

$$\frac{\Delta A}{A} = \frac{|\psi_g(r=0, E \neq 0)\rangle^2}{|\psi_g(r=0, E=0)\rangle^2} - 1 = \eta_A E^2 + O(E^4) \quad (3.7)$$

giving a quadratic shift in E . η_A gives the strength of the shift and is always negative - the mixing with the excited states always reduces the population at the nucleus and thus the hyperfine coupling with it.

In addition to the modulation of the hyperfine coupling there is an effect on the electron g-factor. The g-factor is determined by the spin-orbit coupling and in general depends on the orientation of the applied magnetic field. Due to the valley symmetry of the silicon conduction band this anisotropy is normally averaged out but with the application of an electric field this symmetry is broken, changing the electron's orbit and thus its g-factor. The strength of the effect depends on the axis of electric field. If this axis is along one of the valley axes ([100] crystal axis) then the effect is maximised. If it is along the [111] crystal axis then the effect is equal for all valleys, leaving g-factor unchanged. The g-factor change is given by:

$$\frac{\Delta g_e}{g_e} - 1 = \eta_g(\theta_{BE}, \theta_{BC})E^2 \quad (3.8)$$

where η_g is the Stark g-factor parameter, θ_{BE} is the angle between magnetic and electric fields and θ_{BC} is the angle between the magnetic field and the crystal axis.

Having discussed the theory and background of the Stark shift, I now turn to experimental progress on the subject.

3.3.3 STARK SHIFT MEASUREMENT TECHNIQUES

The first approach to measuring the Stark shift would be to take a field sweep. A field sweep is a standard ESR procedure to determine the magnetic field at which a spin transition occurs for a given microwave frequency. A standard Hahn echo sequence is performed and the intensity of the echo measured for a given before a new magnetic field is set and the procedure repeated. At the correct magnetic field for a spin transition an echo will be recorded, with its intensity diminishing to 0 as the magnetic field moves off resonance. A typical magnetic field sweep for phosphorus doped natural silicon is shown in figure 3.5.

This experiment could be undertaken twice, once with electric field on and once with it off. The Stark shift would produce a change in spin transition frequency which would be observed as a shift in the peaks of the graph. Unfortunately the Stark shift of the spin transition frequency is typically much smaller than the inhomogeneously broadened linewidth of the spin transition, meaning that no shift is visible [5]. Instead Bradbury *et al* used a more subtle technique, harnessing the ability of Hahn echo sequence to refocus inhomogeneous broadening. An electric pulse applied during only one half of a Hahn echo sequence would cause the spins to precess in the magnetic field at different rates when dephasing and rephasing. This shift can then be detected as a phase shift in the echo intensity from the real to the imaginary channel. Changing the length of the applied pulse and recording the echo intensity will introduce an oscillation. The frequency of this oscillation can then be determined using a Fourier transform, thereby giving the Stark shift.

A further effect that must be taken into consideration is the impact of local electric fields. These are present due to local deformations of the crystal lattice, creating different electric environments at each donor. In the presence of an external electric field, the total Stark shift of a given donor is given by:

$$(E_{\text{local}} + E_{\text{ext}})^2 = E_{\text{local}}^2 + E_{\text{ext}}^2 + E_{\text{local}}E_{\text{ext}} \quad (3.9)$$

The inhomogeneity of the local fields would usually provide a simple offset in the phase shift, but the term that is linear in both E_{local} and E_{ext} causes the inhomogeneity to get larger

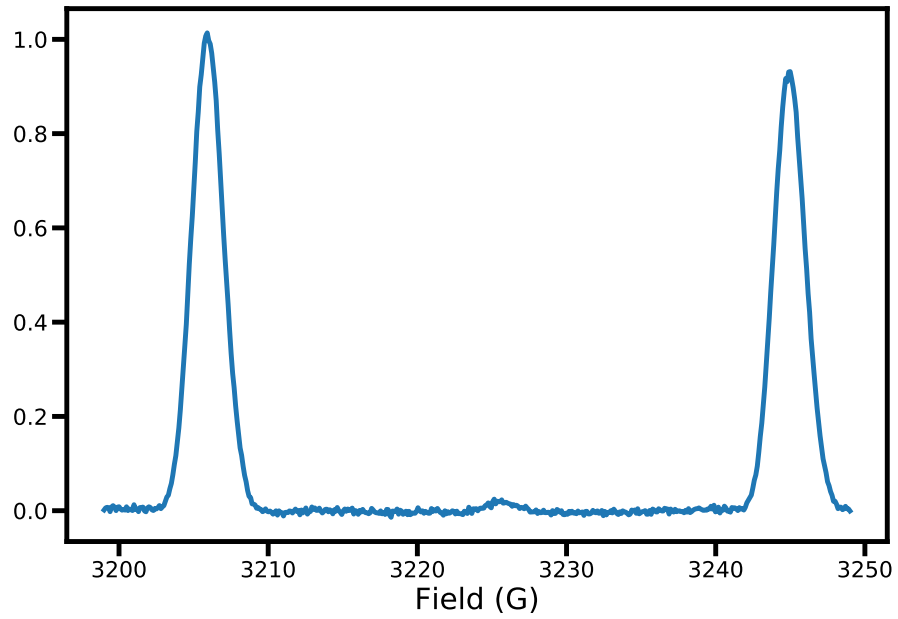


Figure 3.5: Graph showing a standard field sweep to locate spin transitions for electrons bound to phosphorus donors in silicon. Hahn echo intensity is recorded for each magnetic field, with the two large peaks corresponding to electrons bound to the two different phosphorus nuclear spins: $\pm\frac{1}{2}$

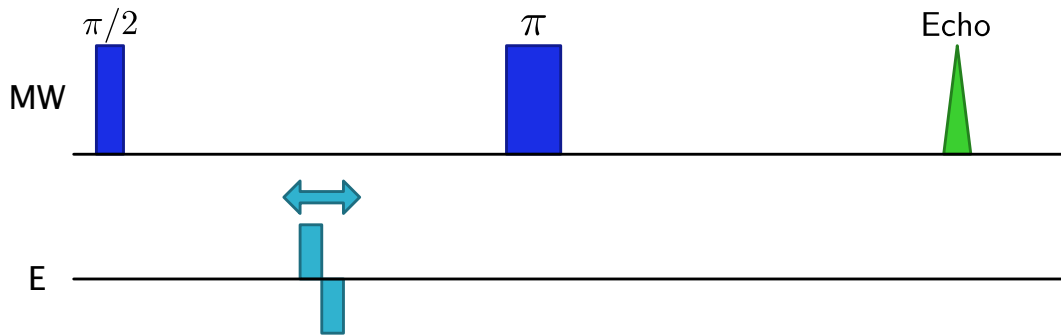


Figure 3.6: The simplest sequence used to measure a Stark shift on an electron. As the pulse length is increased the electron ensemble acquires a different phase during the first half of the echo compared with the second half, seen as a phase shift in the echo from the real to the imaginary channel.

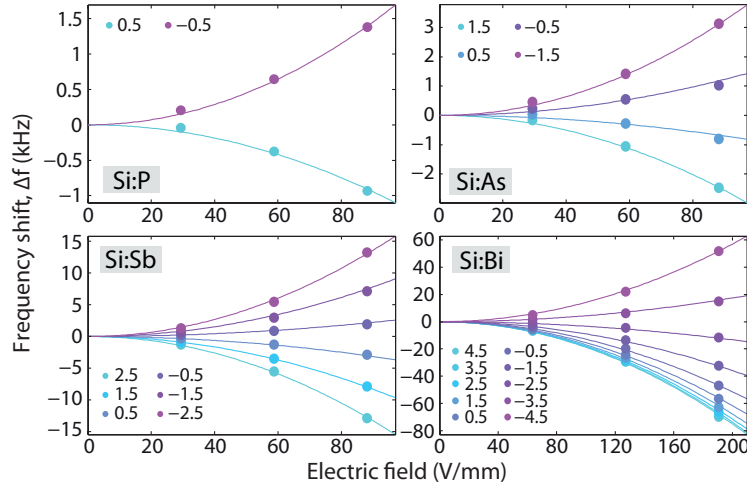


Figure 3.7: These figures demonstrate the frequency shift in the spin transition as a result of the Stark shift, as measured by Wolfowicz *et al* [49]. Notable is the increased rate for higher nuclear spin numbers - this is due to the shift being proportional to the hyperfine coupling, which is in turn proportional to nuclear spin.

as the applied field gets larger. This would result in a rapid decay of the echo signal, but can be avoided by applying a bipolar electric field pulse (i.e. half negative, half positive), a technique implemented by Bradbury *et al* when measuring the Stark shift of antimony donors in silicon [5]. This cancels the linear term but has no impact on the quadratic term. This sequence can be seen in figure 3.6.

3.3.4 STARK SHIFT EXPERIMENTAL RESULTS

Measurements of the Stark shift on all group V donors in silicon were undertaken by Wolfowicz *et al* [31, 49]. The experiment was performed using bulk doped samples of silicon, placed between copper plates. The copper plates were connected to an operational amplifier with an amplification factor of 126. Pulses were generated using an arbitrary wave generator. Results of their measurements are shown in figure 3.7.

These measurements determined the following Stark shift parameter for η_A , with η_g being smaller than the measurement sensitivity:

	^{31}P	^{75}As	^{121}Sb	^{209}Bi
$\eta_A (\times 10^{-3} \mu\text{m}^2/\text{V}^2)$	-2.5 ± 0.5	-1.2 ± 0.1	-3.5 ± 0.05	-0.26 ± 0.05

Wolfowicz *et al* also performed experiments to test conditional control of the spins using Stark shifts. The aim of such an experiment is to shift the transition frequency of the selected

spin by several times its linewidth. This was not possible for the electron due to its broad linewidth even in purified silicon. Instead the experiment was performed on the nuclear transition, which has a much narrower linewidth due to its smaller dipole moment. By applying an electric field at the same time as nuclear spin π pulse, Wolfowicz *et al*, the process is measured as an identity with fidelity $93.3 \pm 2.6\%$. This indicates that it is possible to control the application of pulses to nuclear spin qubits using electric fields as required by the Kane proposal. What is less clear is whether these spin qubits will be sufficiently resistant to any stray electric fields in a scalable quantum computing architecture.

3.3.5 THE NUCLEAR SPIN BATH IN NATURAL SILICON

The presence of ^{29}Si nuclei in natural silicon has been discussed earlier as one of the chief factors impacting qubit coherence times in that medium. Inhomogeneous hyperfine interactions between these spins and addressed electron spins leads to spectral diffusion and reductions in coherence times for qubits in natural silicon. Although most proposals for silicon donor qubit architectures have involved purified silicon to avoid these issues, a proposal has been put forward to use these impurity spins as a quantum register with applications for error correction [47]. From the perspective of the O’Gormann proposal, these spins could present a potential quantum register for data qubits, providing storage for their spin states during long computations. In order to control the interaction between data qubits and the ^{29}Si nuclear spins the Stark shift will be necessary to control the transition frequency of a given spin relative to an external control pulse. Attempting to characterise the Stark shift of the hyperfine coupling between the electron and the ^{29}Si nuclei will be a goal of this report.

3.4 SUMMARY

We have detailed above the theory and current experimental progress for the two main subjects addressed in this report: the impact of laser illumination on spin coherence times in silicon and the Stark shift for Selenium donors and for the coupling to the Si-29 bath. We now move on to the experimental methods

4 EXPERIMENTAL METHODS

4.1 EQUIPMENT

4.1.1 CRYOGENIC AND MICROWAVE INSTRUMENTATION

The experiments in this report were performed in an Oxford Instruments CF935 Helium flow cryostat. A dewar of Helium is connected to this cryostat via a vacuum-insulated transfer arm and kept at approximately 500mBar overpressure, to facilitate cooling without an external pump. Flow into the cryostat is controlled via a valve for coarse temperature control and a heater at the bottom of the cryostat is used along with a PID controller for fine-grained temperature control. A Bruker electromagnet provides a static field of up to 1.5 Tesla for ESR measurements.

For ESR measurements a Bruker E500 X-Band spectrometer is used, with the pulses generated amplified via a travelling wave tube amplifier. The time resolution on this spectrometer is 4ns. Pulses generated enter a Bruker resonator, placed in the cryostat, which has a split ring cavity at the base with the sample at the centre. Microwave pulses entering this cavity generate an oscillating magnetic field at the sample for electron spin control. The resonant frequency of this cavity is fixed at a given temperature but some tuning of its q-factor is possible. This is necessary to ensure that the bandwidth of the cavity is broad enough to admit all control pulses (bandwidth of a pulse is approximates $1/(\text{pulse length})$) and to ensure an appropriate cavity ring-down time. The spectrometer also provides an RF output for nuclear spin control, this is amplified separately and then input into the same resonator.

The electron spin signal is detected through the same channel, the oscillating magnetic field generated by the precessing electrons is demodulated with the same frequency as the control pulse. When the control signal is on resonance this provides two DC signals, one from the in phase (real) component of the demodulation and one from the out of phase (imaginary). This signal decays according to the T_2^* time to provide the characteristic spin echo. This is captured using Bruker's Xepr software, which can integrate under the echo to record changes in intensity.

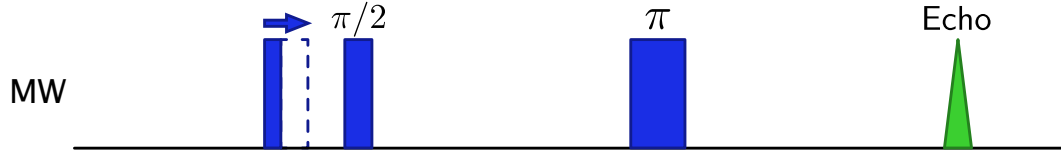


Figure 4.1: The Rabi pulse sequence, used to determine ideal π pulse length at a given power. Creates an oscillation in echo signal as initial pulse length is changed with the rate of oscillation giving the ideal pulse length

4.1.2 LASER

The main laser used in this report is a Toptica DL Pro - a tunable diode laser with a range from approximately 1060nm to 1080nm. This laser can be tuned in two ways: the first is a coarse tuning which is achieved by manually changing the cavity size via a control knob. The second is a fine tuning achieved electronically, this is useful for extremely precise wavelength tuning such as is necessary for bound-exciton experiments or spectroscopy but is not used in this report. The laser has a linewidth of 100kHz and an output power of up to 130mW.

4.2 PULSE SEQUENCES

4.2.1 ESR PULSE SEQUENCES

All experiments in this report are performed using various ESR pulse sequences. The simplest of these is the Hahn echo sequence, described above and depicted in figure 2.2. Several steps are involved to optimise an ESR experiment, the first of which is determining the magnetic field required to excite a spin transition. The microwave frequency is fixed by the cavity so magnetic field must be changed - this is done via a field sweep as described above, the results of which are shown in 3.5. Another critical factor is determining the required length of a π pulse at a chosen power. This is achieved via a *Rabi* sequence, this involves a regular Hahn echo sequence with an additional pulse before the first $\pi/2$ pulse. The length of this pulse is changed and the echo intensity recorded. As this length changes the echo intensity will oscillate, with the frequency of the oscillation giving the correct π pulse length. This sequence is shown in figure 4.1.

Two vital pulse sequences are those that determine the T_1 and T_2 times of a given sample and under given conditions. The pulse sequence to determine T_1 is the *inversion recovery*

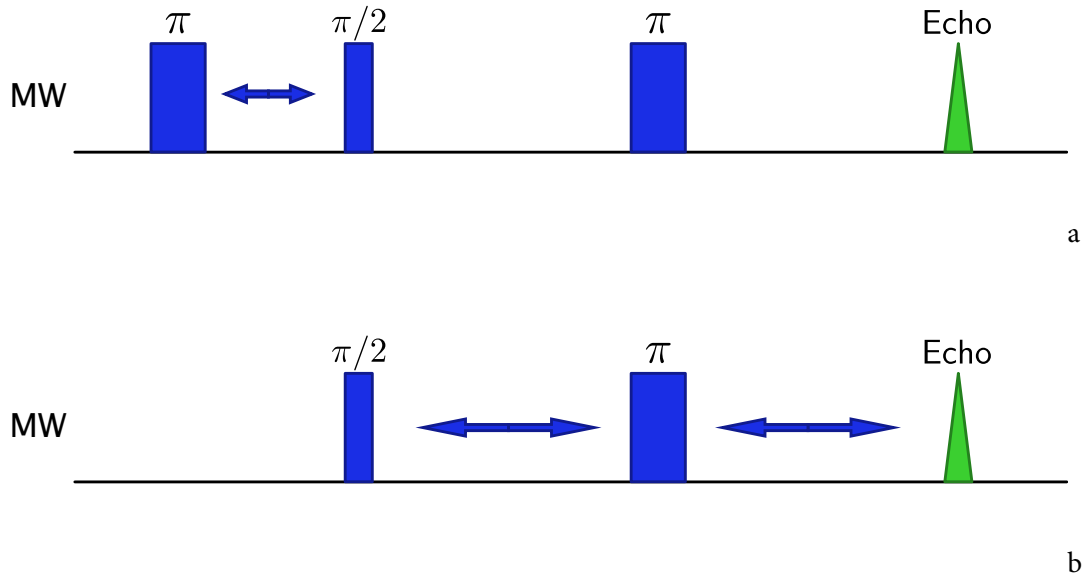


Figure 4.2: Cartoons depicting pulse sequences for measurement of T_1 , a, and T_2 , b. Inversion recovery measures T_1 by inverting the typical spin polarisation with an initial π pulse and increasing the time between this and a Hahn echo sequence. As the time is increased the polarisation has longer to relax to thermal equilibrium, meaning it slowly recovers from fully negative to fully positive in an inverted exponential decay whose time constant is T_1 . T_2 is measured using b, which increases the τ value of the Hahn echo sequence, meaning spins precess in the magnetic field for longer. As they do so they acquire irreversible phase differences leading to the decay of the Hahn echo signal with an exponential decay constant T_2 .

sequence. This consists of a Hahn echo sequence preceded by a π pulse, which inverts the echo signal. The time between the initial π pulse and the Hahn echo sequence is increased, resulting in an inverted exponential decay as the echo recovers from fully inverted to fully positive. This occurs as the polarisation reverts to thermal equilibrium between the initial π pulse and the Hahn echo sequence, with the time constant of the decay giving T_1 .

To determine T_2 the standard experiment is a regular Hahn echo sequence with τ , the time between $\pi/2$ and π , and between π and echo increased. This measures the rate at which spin decoherence occurs - as the spins precess for longer in the magnetic field they gradually acquire irreversible phase differences. As these build up the echo signal decreases exponentially, with the time constant of this decay giving T_2 .



Figure 4.3: (The CPMG dynamical decoupling sequence, which uses successive π pulses to reduce the bandwidth of noise that the donor spins are exposed to, thereby increasing effective decoherence time.)

DYNAMICAL DECOUPLING

A set of pulse sequences all of which attempt to increase coherence times are known collectively as *dynamical decoupling* sequences. At their simplest these add a number of extra π pulses between the initial $\pi/2$ pulse and the echo. Although a full theoretical treatment is complex and well beyond the scope of this work, a physical intuition is relatively simply gained. These pulses reduce the impact of time varying magnetic fields, by effectively narrowing the bandwidth of magnetic noise frequencies that the donor spin is sensitive to [45]. This is done by shortening the time that the electrons precess before they are flipped by a π pulse. Doing this means that slower changing magnetic fields have less of an impact on decoherence - between each reversal of phase acquisition there will have been little field change, meaning that any phase acquired is reversed.

Although more complex sequences exist than simple repetition of π pulses, such as Uhrig Dynamical Decoupling [42], the only one used in this report is the CPMG pulse, a cartoon of which is shown in figure 4.3. Important to note is that the π pulses are applied along an orthogonal rotation axis to the $\pi/2$ pulse as this renders the sequence less susceptible to pulse errors [7, 23].

4.2.2 NUCLEAR PULSE SEQUENCES

Measurements of nuclear spins can be undertaken directly, as is performed in NMR studies, but their significantly weaker signal relative to the electron (due to their much smaller polarisation) makes this technique troublesome. The process undertaken when a couple electron-nucleus system exists is based around ENDOR (Electron Nuclear Double Resonance) sequences. These sequences are based around transferring the electron polarisation

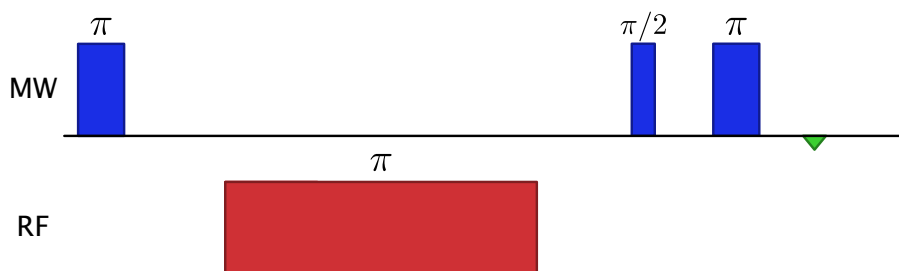


Figure 4.4: This is the simplest sequence with which to identify nuclear spin transitions. The electron spin polarisation is inverted before nuclear π pulse transfers it to the opposite nuclear spin state. This renders the population between the two electron spin states equal, reducing the echo intensity to 0 in the case of a perfect nuclear π pulse.

to the nuclear spin, thereby magnifying the signal to the same level as the electron. The first and simplest of these is the Davies ENDOR sequence, shown in figure 4.4. This sequence first inverts the electron polarisation on one nuclear spin transition before using a nuclear π pulse to transfer it to the opposite nuclear spin transition. This results in an equal polarisation between the two electron spin states so the echo intensity is reduced to 0 in the case of a perfect π pulse.

One potential problem is the long nuclear T_1 time, which can prevent the usual approach to resetting the sample between experiments of waiting for all spins to relax to thermal equilibrium. Continued experiment without relaxation rapidly reduces the signal as the spin transition is saturated. To avoid this a second π pulse (Tidy pulse) is usually added after the echo detection to reset the nuclear spin polarisation to its thermal equilibrium value [24]. This sequence can be used to find nuclear transitions by sweeping the RF frequency of the nuclear π pulse and also to measure the nuclear Rabi frequency by sweeping the pulse length when a transition has been located.

Another useful nuclear sequence is the nuclear echo, which can be used to measure the T_2^* time of the nuclear spins and a variant is used in this report as a means of measuring the Stark shift. This uses a sequence of two nuclear π pulses with a nuclear $\pi/2$ pulse in between. The time between the initial π and $\pi/2$ pulses is kept constant, whilst the time to the final π pulse is swept. This produces a nuclear signal that increases and decays according to the nuclear T_2^* time, with its maximum signal when the pulses are equidistant in time. This is shown in figure 4.5.

The nuclear echo sequence can be used to measure the Stark shift by setting the pulse intervals equal and adding a dipolar electric voltage pulse between two of the pulses. This

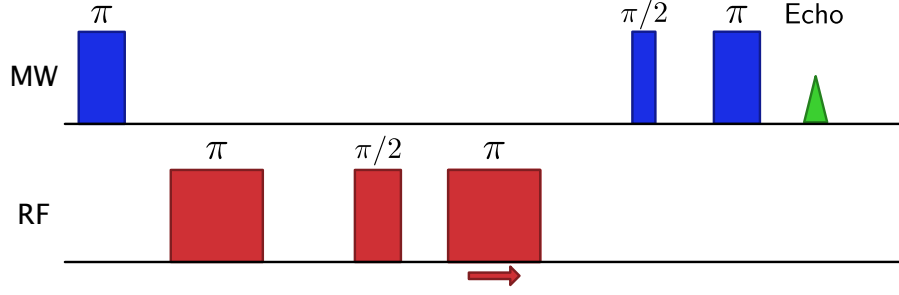


Figure 4.5: Cartoon showing the pulse sequence for a nuclear spin echo

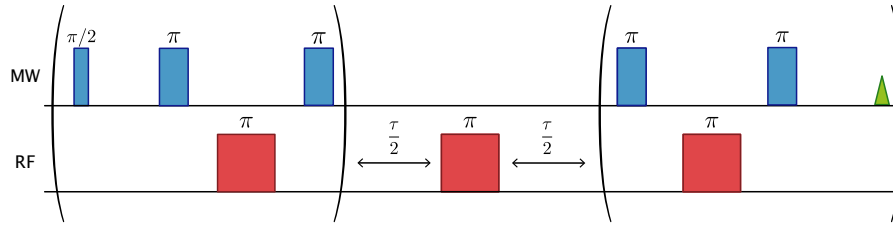


Figure 4.6: Pulse sequence showing the full nuclear coherence transfer. Coherence is created by the first $\pi/2$ pulse before being transferred to the nuclear spin by the subsequent nuclear π and electron π . After a set time the coherence is transferred back to the electron for read out.

causes the nuclear spin to acquire phase depending on the length and strength of the voltage pulse. If the voltage pulse length is swept whilst keeping all other factors constant then an oscillation of the signal is observed, giving the magnitude of the Stark shift.

To measure nuclear T_2 time two pulse sequences can be used, with the most advantageous one being a full nuclear coherence transfer. Whereas most ENDOR experiments only render the nuclear signal in one echo channel (real or imaginary) the full coherence transfer allows both to be meaningful. It is also an important sequence as it allows the storage of quantum information in the nuclear spin, which has a much greater coherence time. This opens up the possibility of using the nuclear spin as a memory for the electron spin [25].

4.3 EXPERIMENTAL SET-UPS

4.3.1 LASER EXPERIMENTS

The set-up for measuring the impact of laser illumination on donors in silicon was relatively simple. The measured sample is placed in a Bruker resonator and loaded into a helium flow

cryostat. The helium flow is initiated and the sample allowed to reach the desired temperature. The Toptica laser beam is initially split using a 90/10 beam-splitter, with the lower power beam subsequently coupled into a fibre. Before fibre coupling the beam must be reflected off two adjustable mirrors to allow sufficient degrees of freedom for optimisation of power input. The fibre passes into a wavemeter, used to determine the output wavelength, and is coarsely tuned to the desired wavelength. The laser beam is not visible so is aligned to the cryostat window via an infrared-sensitive camera. For fine-tuning of the alignment, two approaches were used. The first is to place the sample in between two metallic contacts connected to a lock-in amplifier with a small oscillating voltage applied across the plates. The laser spot location is fine tuned via adjustable mirrors until the current measured by the lock-in amplifier is maximised. An alternative technique, not requiring the additional components but more taking more time, is to maximise the effect of the laser. This is done by measuring T_1 time of the sample repeatedly and adjusting the laser to minimise this measurement (indicating that the effect of the laser is maximised).

The laser output power can be controlled by changing the amplitude of the control voltage. This output power can be measured using a power metre and set to the desired value. Although this approach is appropriate for high powers, the limited resolution of the power metre ($\approx 0.2\text{mW}$) makes it inappropriate for lower powers. To reach lower laser powers at reasonable errors ND filters are used. These are valued from ND 1.0 - 4.0 and ND 0.1-0.6 in two separate filter wheels. The power is set via control voltage to a stable value and ND filters are then used to adjust to the power at the sample. Manufacturer values for transmission at the relevant wavelength are then used to calculate exact powers as these vary slightly with wavelength.

In all experiments on laser illumination the sample used was a float zone natural silicon sample doped at $6 \times 10^{15}\text{cm}^{-3}$ and sized at $1.5 \times 1.5 \times 10\text{mm}$.

4.3.2 STARK SHIFT EXPERIMENTS

The Stark shift measurement set-up requires placing the sample in between two copper electrodes designed to cover the sample. The electrodes are placed in direct contact with the sample and held in place by thread tape. These electrodes are each soldered to a copper wire allowing the application of voltage pulses. Bi-polar pulses are generated using an AWG at up to $\pm 2\text{V}$ and subsequently amplified using an operational amplifier with a gain of $60\times$. Pulses are simultaneously monitored on an oscilloscope during application to measure the exact voltage being applied.

5 RESULTS

In this chapter we will address the results gained so far. Looking first at the impact of laser illumination on coherence times before examining the impact of the Stark shift on selenium donors in purified silicon and the hyperfine coupling of phosphorus donors to ^{29}Si nuclei in natural silicon.

5.1 ILLUMINATION INDUCED DECOHERENCE

5.1.1 INITIAL MEASUREMENTS

The first step undertaken before any laser illumination occurs is to characterise the sample's T_1 and T_2 times 'in the dark' at the measurement temperature. Experiments were performed at 8k and 7k, with typical T_1 and T_2 decays shown in figure 5.1. The inversion recovery has been fitted with a standard exponential decay whilst the T_2 decay has had a stretched exponential decay applied. The time constants of these decays give the T_1 and T_2 times with errors in the fit used to establish errors in their values. The stretched exponential decay of T_2 indicates the presence of spectral diffusion. T_2 decays with dynamical decoupling applied do not have this stretch factor as they are isolated from spectral diffusion. A problem with the results presented here is a variation in the time constant for the decay in the dark, with 2.77ms found in the high power experiments, whilst 6.4ms was found during the low power experiments. These results are therefore presented separately to avoid confusion. It is possible that this is attributable to different flow rates in the helium cryostat, meaning that use of a dry cryostat, which offers much greater temperature precision, would be beneficial. At 7k T_1 was $32 \pm 0.1\text{ms}$ and T_2 was unchanged.

5.1.2 BI-EXPONENTIAL INVERSION RECOVERY

A set of high power measurements have been taken at powers between 2mW and 130mW, at wavelengths 1060nm, 1070nm and 1080nm, and at temperatures of 7k and 8k. At each power and wavelength 3 measurements were made: T_1 , T_2 and T_2 whilst using a 4π pulse dynamical decoupling sequence - CPMG. An initial observation is that there is a strongly bi-exponential shape to the inversion recovery, requiring a fit of the form:

5 Results

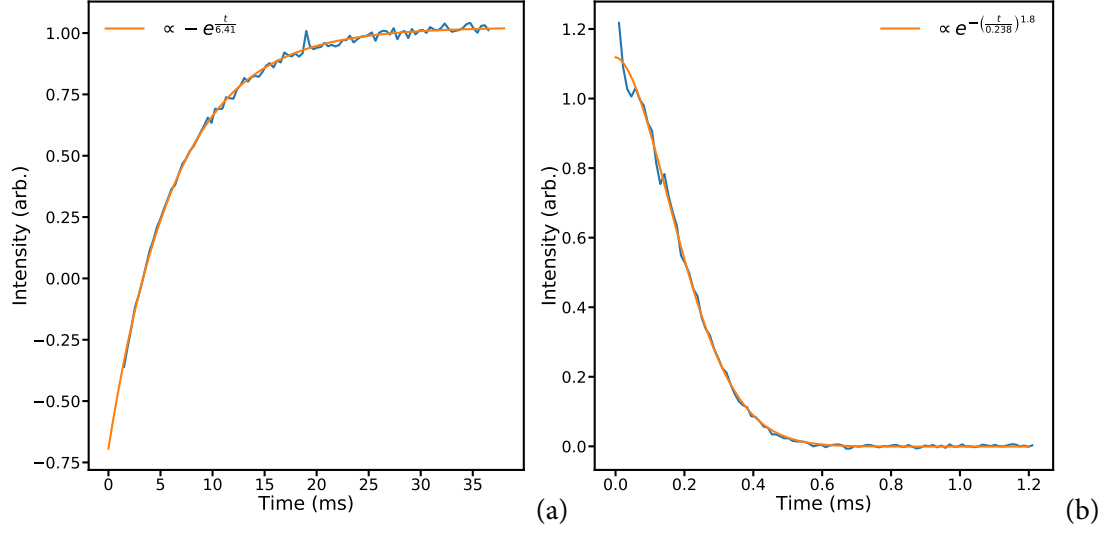


Figure 5.1: Typical T_1 and T_2 decays showing the inversion recovery for T_1 and the characteristic stretched exponential for T_2 , indicating the presence of spectral diffusion.

$$ae^{\frac{t}{T_{1a}}} + be^{\frac{t}{T_{1b}}} \quad (5.1)$$

this is clearly seen in figure 5.2.

Of the two time constants that describe the decay, one is significantly longer than the other and at low powers is close to the T_1 in the dark. This suggests that there is a distribution of the illumination effect throughout the sample, with less affected parts relaxing more slowly than others. This becomes more obvious when comparing the two time constants over a range of powers, as seen in figure 5.3. This shows that the lower T_1 has a strict inverse polynomial dependence on laser power, whilst the longer T_1 cannot be similarly fit as it appears to saturate at lower powers. Given this, it seems prudent when trying to determine the relationship between the incident light parameters and relaxation behaviour to use the shorter of the two time constants where a bi-exponential fit has been applied. In the case of a set of data qubits close to the silicon surface, as is suggested in [29], these qubits would be exposed to illumination and not shielded as appears to be the case in the long T_1 case.

5.1.3 HIGH POWER WAVELENGTH COMPARISON

EFFECT ON T_1

Measurements comparing behaviour of T_1 , T_2 and dynamical decoupling T_2 were performed at 3 wavelengths: 1058nm, 1070nm, and 1080nm. The lowest of these represents photon en-

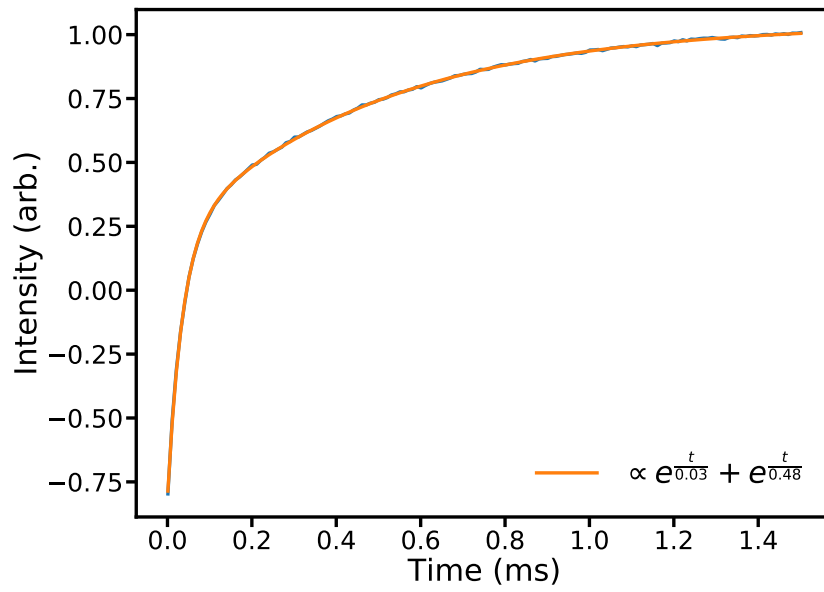


Figure 5.2: Inversion recovery at 8k and under 79mW illumination at 1070nm. Of note is the strongly bi-exponential nature of the decay, with two distinct time constants describing it. One significantly longer than the other. A possible explanation for this is that the laser illumination is not affecting all parts of the sample. This is not unexpected as the sample is quite large, as described in section [4.3.1](#)

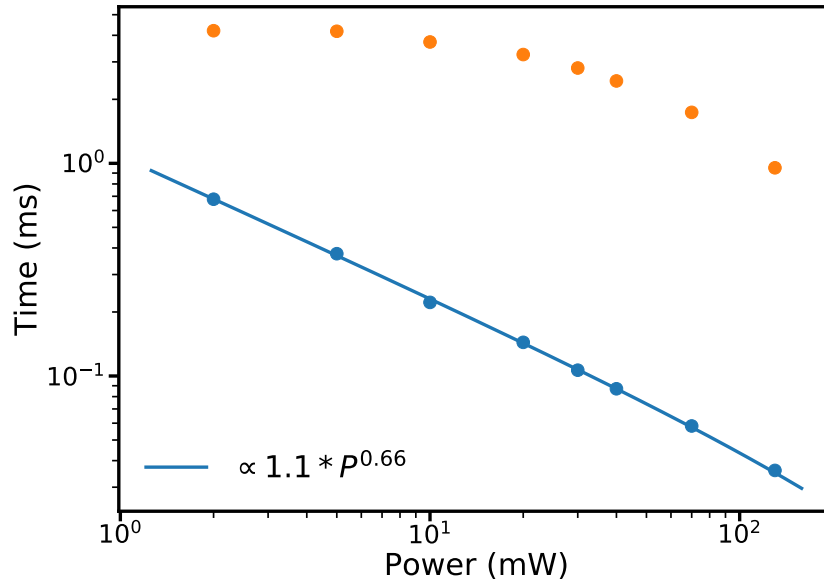


Figure 5.3: Figure shows the two constants for bi-exponential relaxation decay whilst under laser illumination at 1070nm and at 8k. The shorter T_1 constant is well fit with a $\frac{1}{P^{0.66}}$ line. A similar fit cannot be applied to the longer T_1 constant, which appears to demonstrate saturation behaviour at the lower illumination powers.

ergies at approximately the band gap energy of silicon. As such, it would be expected that this wavelength would have a stronger effect than the other two as the free carrier generation rate would be significantly higher. This factor has previously been postulated as the dominant process affecting relaxation rates of donor electrons. Figure 5.4 shows the relationship between relaxation time and laser power for three wavelengths, fitted according to A/t^α . The power for each wavelength is $0.73 \pm .002$, $0.68 \pm .0002$ and $0.68 \pm .003$, in order of increasing wavelength. Measurements were also taken at 2mW and 5mW but are not included here as the large error in their measurements makes them unsuitable for comparison between data sets. What is clear from the above graph is that there is an observable difference between the case of 1058nm illumination and the two higher wavelengths. This is to be expected given that 1058nm is at approximately the silicon band gap, meaning that absorption of photons will be higher and free carrier generation significantly higher than with less energetic photons. Although the higher wavelengths have a lesser effect, there is still a strong reduction in relaxation times. The similarity between the effects suggest that the mechanisms responsible for the increased rate do not have a strong dependence on individual photon energy once the band-gap is passed, instead the power of the incident illumination is dominant.

The impact of illumination on relaxation rates observed here is in line with predictions. Increased wavelength results in a slower relaxation rate at equivalent powers, with a more

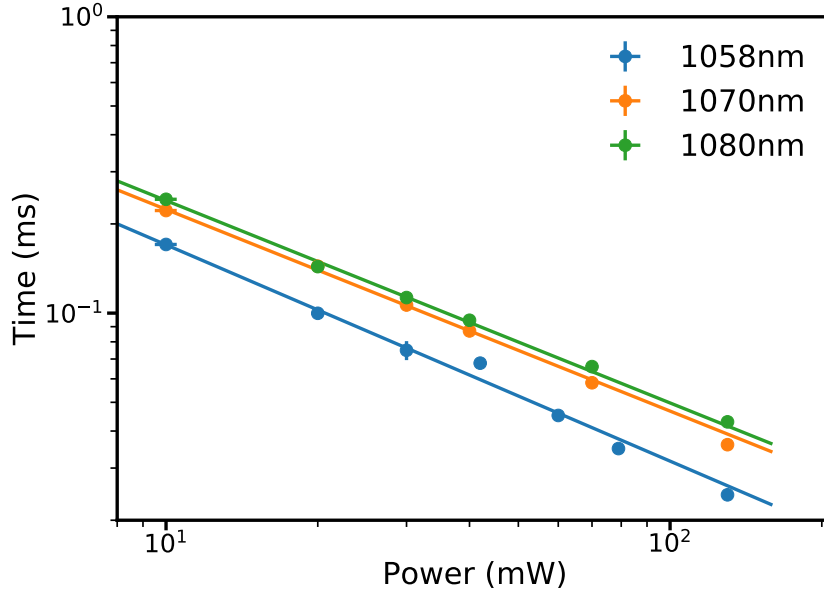


Figure 5.4: Figure shows the relationship between laser power and relaxation time for 3 different wavelengths: 1058nm, 1070nm and 1080nm.

significant change being observed as the silicon band gap energy is crossed. Relaxation rates follow a a/P^α

EFFECT ON T_2

Whilst the T_1 time is important for quantum information processing, as it ultimately limits computation time, T_2 is in most cases the limiting factor in qubit coherence. The mechanisms that limit T_2 in spins were discussed in section 3.1.2. Of particular worry is that a significant number of free electrons in the silicon conduction band could create time dependent magnetic fields at the observed donor spins. If this is the case then there could be an impact on the T_2 time beyond the effect of reduced T_1 . Figure 5.5 shows how T_1 and T_2 vary with laser power for 1058nm and 1070nm. What is clear in both cases is that there does not appear to be a significant effect beyond T_2 being limited by T_1 . In both graphs it is clear at the lower powers that T_2 is beginning to saturate to the value in the dark of $220\mu s$. The fact that there is no clear difference between the effects in the 1058nm case and the 1070nm case is interesting. It suggests that, although there is clearly a greater magnitude of effect in the lower wavelength case, if the mechanism is different then it has no impact on T_2 above and beyond the extra T_1 limitation.

The next question to be answered is whether the T_1 time will demonstrate a similar saturation behaviour as laser power is reduced as is demonstrated by T_2 . To see this lower powers

5 Results

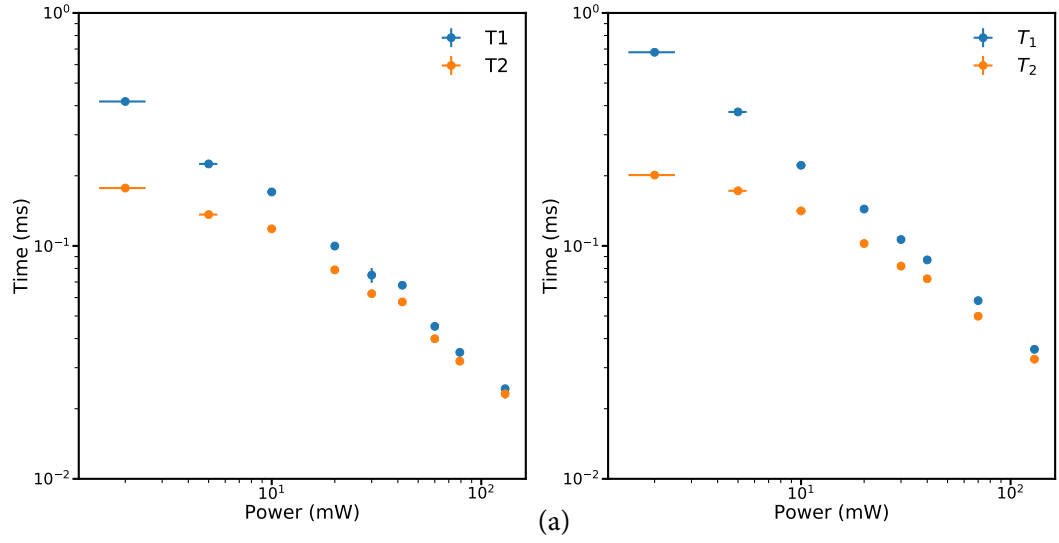


Figure 5.5: Figures showing how both T_1 and T_2 vary with laser power, presented on the same scale for ease of comparison. At high powers T_1 is observed to be close to T_2 , essentially limiting it.

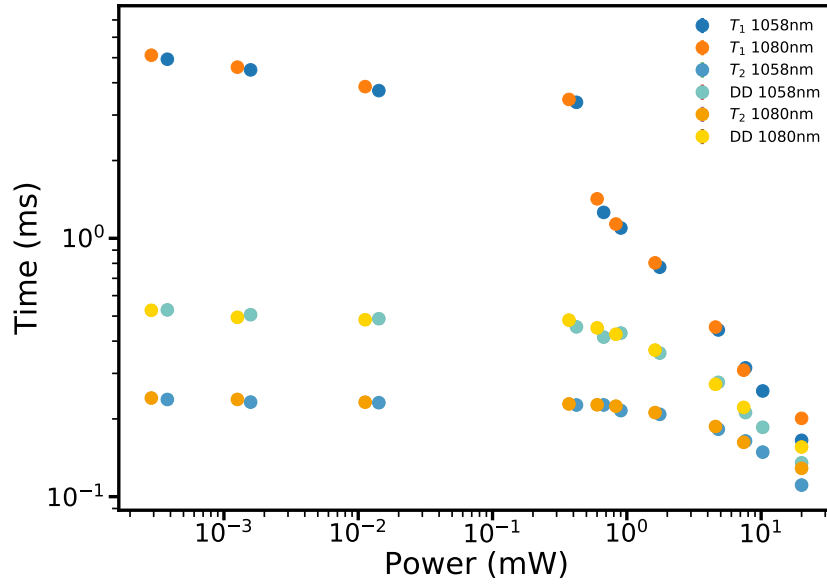


Figure 5.6: Figure shows the impact of laser illumination at low power and at wavelengths of 1058nm and 1080nm. T_1 is observed to saturate at very low laser powers, as it becomes close to the T_1 in the dark. Included is the coherence time for a 4π pulse dynamical decoupling sequence. This shows the expected increase in decoherence time at lower powers and continues to have an advantage over a traditional Hahn echo sequence as both begin to be reduced. Small differences in power at equivalent data points are due to the transmission of ND filters varying slightly with wavelength.

must be used, achieved as described in section 4.3.1 through the use of ND filters. The results are shown in figure 5.6. These demonstrate that the T_1 does indeed saturate towards the dark T_1 at very low powers. Of interest is the behaviour of the T_2 time as the T_1 time starts to be reduced significantly. The T_2 time clearly starts to decrease *before* it is strictly limited by T_1 . Several factors could explain this. The first possibility is that the creation of free carriers promoted from the valence band is causing extra magnetic field noise at donor sites, reducing their T_2 time. The difficulty with this particular mechanism is that there appears to be very little difference, at these low powers, between the T_2 times at the different wavelengths. Were this to be a significant effect then one would anticipate that it would be noticeably stronger in the lower wavelength case. The alternative factors are T_1 related, were discussed in section 3.1, and account well for the observed behaviour. As relaxation rate increases, decoherence rate is also observed to increase before being strictly limited by the relaxation rate. This is due in the main to the additional spectral diffusion processes as a result of neighbouring donor electron spin flips. As seen in figure 5.6, dynamical decoupling gives an advantage over a Hahn echo sequence for decoherence time. As this is a natural silicon sample the advantage in the dark is to be expected, a small advantage remains even when the dynamical decoupling T_2 is shorter than the Hahn echo. This suggests that the 4 pulse echo sequence is providing some protection from the mechanisms causing the increased decoherence rate - likely the spectral diffusion processes associated with an increased relaxation rate.

The results here allow one important conclusion - there do not seem to be significant decoherence effects caused by laser illumination beyond the impact of an increased relaxation rate. This is an important as it demonstrates that laser based read-out of measurement qubits is possible without destroying the quantum information held in data qubits, as long as power is sufficiently low. To explore whether the impact on relaxation rates at a given laser power can be reduced I turn now to examine results at a lower temperature - 7k.

5.1.4 TEMPERATURE COMPARISON

A temperature comparison is useful primarily to give insight into the mechanism of increased relaxation rate. A first expectation is that relaxation rate will begin to saturate at lower laser powers at lower temperatures, in line with the longer dark relaxation rate. Particularly revealing will be a direct comparison between relaxation rates at the same wavelength and power, but at different temperatures. If these are the same then it would suggest that whatever mechanism affecting the relaxation rate is temperature independent - potentially ruling out heating as a cause. Figure 5.7 shows how T_1 changes with laser power at 1058nm and at 7k and 8k, with T_1 s in the dark of 2.77ms and 32.2ms respectively.

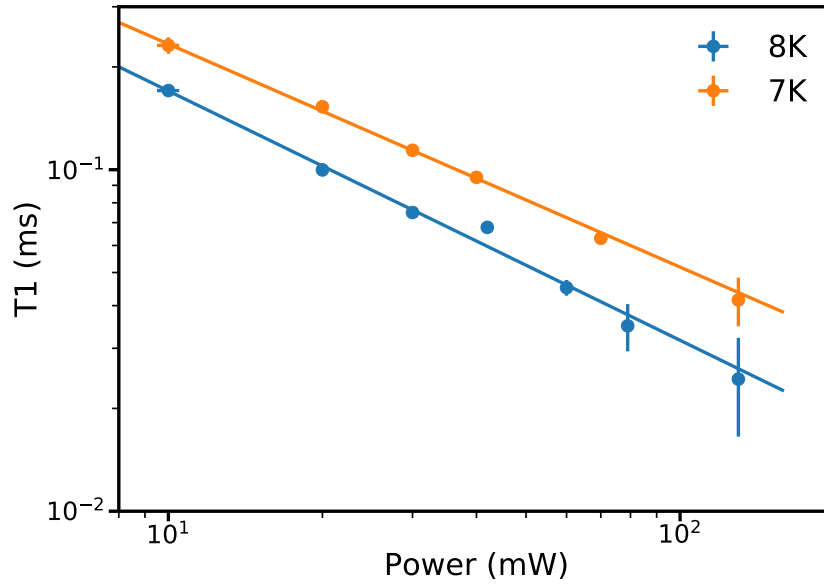


Figure 5.7: Figure shows how T_1 changes with laser power at 1058nm and for 8k and 7k, with respective dark T_1 s of 2.77ms and 32.2ms. It is interesting to note that there is a clear increase in relaxation rate at 8k vs 7k. This suggests that the mechanism by which the laser acts has some temperature dependence.

What is immediately clear from this comparison is that the laser is not a purely limiting factor. The 8k fit has the same parameters as given above, whilst the 7k fit has a power of 0.65 ± 0.002 . At 7k there is a clear increase in T_1 at the same laser power relative to 8k, suggesting that whatever mechanism is reducing relaxation time does indeed have a temperature dependence. I will now address the mechanisms that are potentially responsible for the observed effects, concentrating on heating.

5.1.5 HEATING AS A MECHANISM OF RELAXATION

Estimating the potential effect of heating as a result of laser illumination is complex. The first factor affecting such an estimation is that the temperature sensor that is used to control the cryostat is not located on the sample so the highly localised heating caused by a laser would likely not be detected. Beyond this, estimations are made difficult by the somewhat scarce information on light absorption at cryogenic temperatures in silicon. The reason that heating is presented as a potential explanation for the observed relaxation effects is the extremely low heat capacity of silicon at cryogenic temperatures, as predicted by the Debye model [10]. This means that only a small amount of energy is required to effect significant heating in silicon. Also relevant is that silicon is a poor photo-emitter, meaning that any infra-red radiation

absorbed is likely to end up as heat rather than emitted photons. Calculating potential heat rises is made difficult by the scarcity of literature on the absorption coefficient of silicon at low temperatures. Studies have concentrated on silicon at room temperature due to its use in solar cells and have tended to assume that low-temperature, below band-gap absorption will be low due to the scarcity of phonons to assist transitions. Interest has been peaked recently due to the possibility of taking advantage of the anticipated high transmission qualities of silicon at low temperatures for use as an interferometer in a gravitational wave detector [11]. One study in particular provides a useful insight, although not a directly comparable one. This measured the absorbance of silicon at 6k by monitoring its temperature increase under illumination by a 1550nm laser. Results of this experiment show a much greater absorption than anticipated, with the measured result being the same at 6k as at room temperature: 0.030cm^{-1} . Taking this figure as a guideline, it can be estimated that approximately 0.5% of incident light is absorbed by the sample in these experiments. Harder to estimate is the rate at which the sample is cooled in the cryostat, which will determine how much extra energy it holds in equilibrium with the laser turned on. In [11] the sample was observed to increase in temperature as long as the laser was turned on. It was, however, poorly thermally coupled to its cooling environment and it seems likely that a sample in direct contact with helium flow will reach an equilibrium temperature value. Here I make the assumption that approximately 1% of the laser power is retained in the sample at equilibrium, adding to its temperature. This figure can be used along with heat capacity, taken from [12, 16], to calculate the expected temperature for a given laser power. Using this temperature along with the equations in section 3.1 allows an estimation of T_1 and T_2 times at given laser powers. A further potential contributor to relaxation rates is donor ionisation - unpaired electrons on the donor being excited to the conduction band by an incident photon. This would be registered first as a loss in signal and then a relaxation back to thermal equilibrium as the donor is recaptured by an ionised donor. This process also contributes to heating of the sample - an electron excited to the conduction band *thermalises* (relaxes to the energy minimum of the conduction band) rapidly - but this effect is already accounted for in the heating calculation. The cross section for this process is predicted to be low - peaking at $17 \times 10^{-16}\text{cm}^{-2}$ and significantly lower at the wavelengths used in these experiments [34, 36]. Following [34], a figure of $1.5 \times 10^{-16}\text{cm}^{-2}$ is used to calculate rate of donor ionisation with power. Given these parameters, a simulation of relaxation rate based on laser power, when accounting for donor ionisation rates and heating effects is given in figure 5.8.

The results shown here, whilst by no means conclusive, suggest that heating is a potential cause of the observed effects. At higher powers the heating effect appears to increase faster in the simulation than in the experimental results but further work will be required to refine

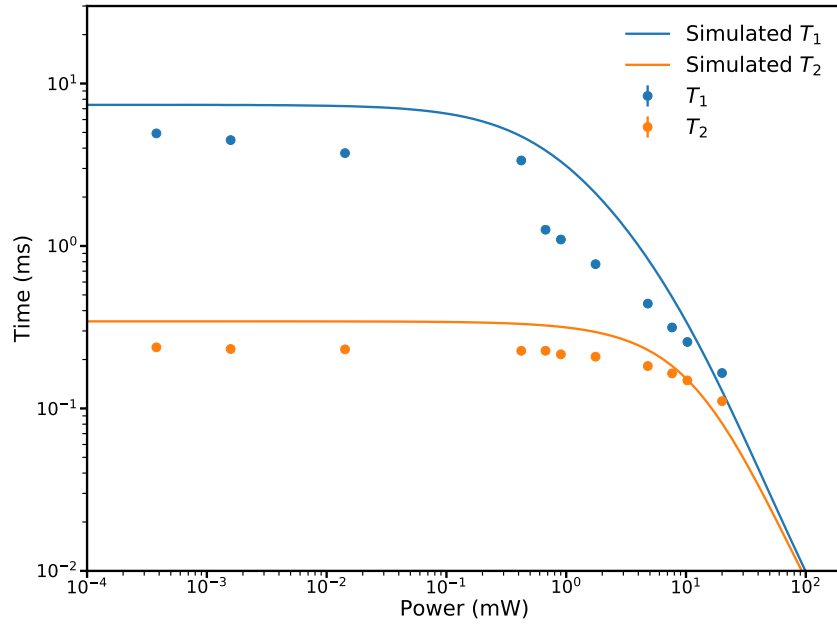


Figure 5.8: Figure showing the simulated T_1 and T_2 as a function of laser power at 8k when taking account of potential heating, alongside low power data taken at the same temperature. Data for T_1 and T_2 calculated using heat capacity of silicon at these temperatures alongside equations shown in section 3.1.

these figures. Heating does appear to account quite well for the observed discrepancy in T_1 and T_2 times at each temperature.

I have not discussed the mechanism that Feher and Gere identify as the most prominent in their results: the double spin exchange between free electron, donor electron and donor nucleus. This process, although mentioned by Feher and Gere, is given no explicit form. A qualitative argument is used to explain why it accounts for the observed behaviour of electron relaxation time under illumination. As such it is difficult to incorporate such a mechanism into my simulations. One question would be whether this mechanism would demonstrate the temperature dependence that has so far been observed, with relaxation occurring more slowly at lower temperatures but under the same illumination. It is possible that the lower thermal velocity of free electrons at lower temperatures could account for the discrepancy, giving a smaller number of double scattering events per second. This presents an excellent next step for this work: determining both the density of free carriers at each wavelength and using this to provide an account of the scattering rate of electrons on donors.

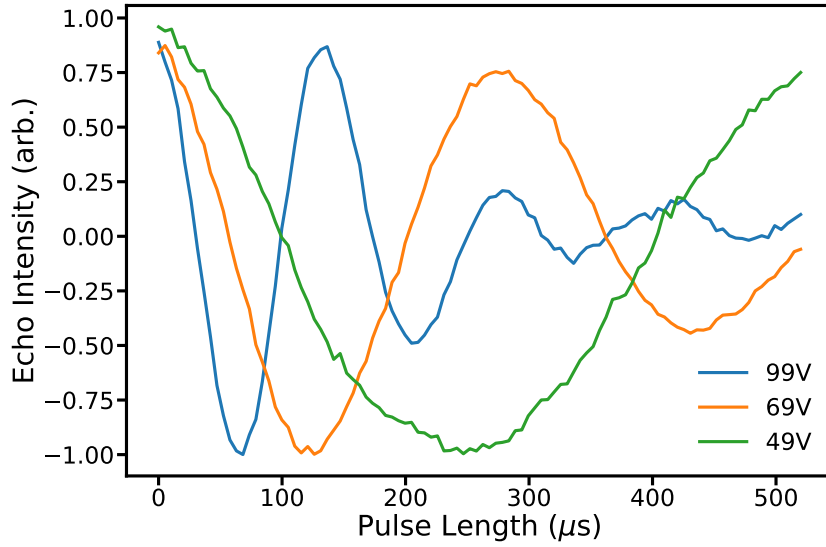


Figure 5.9: Figure showing the Stark shift in bismuth as a result of bi-polar voltage pulses applied in one half of a Hahn echo sequence causing a phase shift in the electron precession. Oscillations frequency is proportional to the square of the voltage applied. The decay in the signal as the pulse length increases is a result of the inhomogeneous linear Stark term causing the loss of phase coherence.

5.2 STARK SHIFT EXPERIMENTS

5.2.1 STARK SHIFT ON SELENIUM DONORS

Observing the Stark shift proved challenging initially, with a replication of the previous experimental set-up not yielding the results that were expected when the set-up was tested on previously investigated systems. This proved to be due to a flaw in the positioning of the plates used to produce an electric field relative to the sample. Contact between the plates and the sample was required to observe a Stark shift. Once the set-up issues had been established a Stark shift was observed in Bismuth, replicating a prior experiment, as seen in figure 5.9.

This figure shows the oscillation in phase of the echo signal as the voltage pulse length is increased. The oscillation is proportional to E^2 , causing the increase in oscillation rate as voltage is increased. The decay in the oscillations, particularly clear in the 99V case, is caused by the contribution of inhomogeneous linear electric field terms. Strain is a strong contributor to this effect meaning that excessively firm contact between plates and sample results in the rapid decay of the signal.

Difficulties have been encountered measuring the Stark shift on selenium, in part due to its expected low value. As discussed in section 3.3, the Stark shift is caused by a mixing between

the ground state of the electron on the donor and higher energy levels leading to a modulation of the Hyperfine coupling between electron and nucleus. The gap to first excited state in selenium (as a deep donor) is significantly larger than in the shallow donors in silicon. For example: phosphorus has a gap to the first excited state of 10.5meV, bismuth 33.8meV; selenium has a gap of 429meV [22, 26]. As yet no Stark shift has been observed in Selenium, using pulses of up to 800 μ s long at ± 99 V. By taking the maximum possible unobserved phase shift as being equal to the signal to noise ratio of the obtained data it is possible to obtain a value for η_A , the hyperfine Stark shift coefficient, of 0.7×10^{-7} . I am not yet fully confident in this result due to several issues with the current experiment. The first of these is that it has been shown to be extremely sensitive to experimental set-up - strain and lack of contact between the plates and the sample rendering the results inaccurate. The sample being used for these experiments is quite large, being 4mm \times 4mm \times 2mm. This means that the plates cannot cover the entirety of the sample and remain able to fit in the spectrometer cavity. The presence of selenium also means that electrons preferentially populate these impurities, rather than any phosphorus impurities in the sample. This makes it hard to verify the Stark shift on a phosphorus transition before measuring a selenium transition. One possible approach would be to populate the phosphorus impurities by using an above band gap laser pulse - a technique used in the group previously [26]. This would allow verification of the strength of the Stark shift on phosphorus prior to measuring it on selenium - allowing confidence in the experimental set-up.

5.2.2 STARK SHIFT ON ^{29}Si NUCLEI

BIBLIOGRAPHY

1. D. Aharonov and M. Ben-Or. “Fault-tolerant quantum computation with constant error”. *Proceedings of the twenty-ninth annual ACM symposium on Theory of computing - STOC '97*, 1997, pp. 176–188. ISSN: 1533-. DOI: [10 . 1145/258533 . 258579](https://doi.org/10.1145/258533.258579). arXiv: [9906129v1](https://arxiv.org/abs/9906129v1) [[arXiv:quant-ph](#)].
2. C. J. Ballance et al. “Laser-driven quantum logic gates with precision beyond the fault-tolerant threshold”. *arXiv preprint*, 2015, pp. 1–12. arXiv: [1512 . 04600](https://arxiv.org/abs/1512.04600). URL: [http : //arxiv.org/abs/1512.04600](http://arxiv.org/abs/1512.04600).
3. D. G. Baranov et al. “Modifying magnetic dipole spontaneous emission with nanophotonic structures”. *Laser and Photonics Reviews* 11:3, 2017. ISSN: 18638899. DOI: [10 . 1002/lpor.201600268](https://doi.org/10.1002/lpor.201600268).
4. R. Barends et al. “Digital quantum simulation of fermionic models with a superconducting circuit”. *Nature Communications* 6:May, 2015, p. 7654. ISSN: 2041-1723. DOI: [10 . 1038 / ncomms8654](https://doi.org/10.1038/ncomms8654). arXiv: [1501 . 07703v1](https://arxiv.org/abs/1501.07703v1). URL: [http : // www . nature . com / ncomms / 2015 / 150708 / ncomms8654 / full / ncomms8654 . html{\%}5Cnhttp : //www.nature.com/doifinder/10.1038/ncomms8654](http://www.nature.com/ncomms/2015/150708/ncomms8654/full/ncomms8654.html{\%}5Cnhttp://www.nature.com/doifinder/10.1038/ncomms8654).
5. F. R. Bradbury et al. “Stark tuning of donor electron spins in silicon”. In: *AIP Conference Proceedings*. Vol. 893. 2007, pp. 1093–1094. ISBN: 9780735403970. DOI: [10 . 1063/1 . 2730277](https://doi.org/10.1063/1.2730277). arXiv: [0603324](https://arxiv.org/abs/0603324) [[cond-mat](#)].
6. S. B. Bravyi and A. Y. Kitaev. “Quantum codes on a lattice with boundary . \square ”. 96, 2008, pp. 1–6. arXiv: [9811052v1](https://arxiv.org/abs/9811052v1) [[arXiv:quant-ph](#)].
7. H. Y. Carr and E. Purcell. “Effects of Diffusion on Free Precession in Nuclear Magnetic Resonance Experiments”. *Physical Review Letters* 94:3, 1954, pp. 630–638. ISSN: 13672630. DOI: [10 . 1126/science.1231675](https://doi.org/10.1126/science.1231675). arXiv: [arXiv:1011.1669v3](https://arxiv.org/abs/1011.1669v3).
8. J. R. Chelikowsky and M. L. Cohen. “Electronic structure of silicon”. *Physical Review B* 10:12, 1974, pp. 5095–5107. ISSN: 01631829. DOI: [10 . 1103/PhysRevB . 10 . 5095](https://doi.org/10.1103/PhysRevB.10.5095). arXiv: [arXiv:1011.1669v3](https://arxiv.org/abs/1011.1669v3).
9. D. J. Christle et al. “Isolated electron spins in silicon carbide with millisecond coherence times”. *Nature Materials* 14:2, 2014, pp. 160–163. ISSN: 1476-1122. DOI: [10 . 1038 / nmat4144](https://doi.org/10.1038/nmat4144). arXiv: [1406 . 7325](https://arxiv.org/abs/1406.7325). URL: [http : //www.nature.com/doifinder/10 . 1038/nmat4144](http://www.nature.com/doifinder/10.1038/nmat4144).
10. P. Debye. “Zur Theorie der spezifischen Wärmen”. *Annalen der Physik* 344:14, 1912, pp. 789–839. ISSN: 1521-3889. DOI: [10 . 1002/andp.19123441404](https://doi.org/10.1002/andp.19123441404). URL: [http://dx . doi.org/10.1002/andp.19123441404](http://dx.doi.org/10.1002/andp.19123441404).

11. J. Degallaix et al. "Measurement of the optical absorption of bulk silicon at cryogenic temperature and the implication for the Einstein Telescope". *Classical and Quantum Gravity* 31:18, 2014. ISSN: 13616382. DOI: [10.1088/0264-9381/31/18/185010](https://doi.org/10.1088/0264-9381/31/18/185010).
12. P. D. Desai. *Thermodynamic Properties of Iron and Silicon*. 1986. DOI: [10.1063/1.555761](https://doi.org/10.1063/1.555761).
13. G. Feher. "Electron spin resonance experiments on donors in silicon. I. Electronic structure of donors by the electron nuclear double resonance technique". *Physical Review* 114:5, 1959, pp. 1219–1244. ISSN: 0031899X. DOI: [10.1103/PhysRev.114.1219](https://doi.org/10.1103/PhysRev.114.1219).
14. R. P. Feynman. "Simulating physics with computers". *International Journal of Theoretical Physics* 21:6-7, 1982, pp. 467–488. ISSN: 00207748. DOI: [10.1007/BF02650179](https://doi.org/10.1007/BF02650179). arXiv: [9508027 \[quant-ph\]](https://arxiv.org/abs/quant-ph/9508027).
15. E Gere and G Feher. "Electron Spin Resonance Experiments on Donors in Silicon. II. Electron Spin Relaxation Effects". *Physical Review* 114:5, 1959, p. 1245. ISSN: 0031899X. DOI: [10.1103/PhysRev.114.1245](https://doi.org/10.1103/PhysRev.114.1245).
16. V. M. Glazov and A. S. Pashinkin. "The Thermophysical Properties (Heat Capacity and Thermal Expansion) of Single-Crystal Silicon". *High Temperature* 39:3, 2001, pp. 413–419. ISSN: 1608-3156. DOI: [10.1023/A:1017562709942](https://doi.org/10.1023/A:1017562709942).
17. J. P. Gordon and K. D. Bowers. "Microwave spin echoes from donor electrons in silicon". *Physical Review Letters* 1:10, 1958, pp. 368–370. ISSN: 00319007. DOI: [10.1103/PhysRevLett.1.368](https://doi.org/10.1103/PhysRevLett.1.368).
18. D. Gottesman. "Stabilizer Codes and Quantum Error Correction". 2008, 1997. ISSN: 0163-6804. DOI: [10.1017/CB09781107415324.004](https://doi.org/10.1017/CB09781107415324.004). arXiv: [9705052 \[quant-ph\]](https://arxiv.org/abs/quant-ph/9705052).
19. E. L. Hahn. "Spin Echoes". *Physical Review* 80:4, 1950, pp. 580–594.
20. B. E. Kane. "A silicon-based nuclear spin quantum computer". *Nature* 393:6681, 1998, pp. 133–137. ISSN: 0028-0836. DOI: [10.1038/30156](https://doi.org/10.1038/30156). URL: <http://www.nature.com/doifinder/10.1038/30156>{\%}5Cnpapers2://publication/doi/10.1038/30156.
21. G. Q. Liu et al. "Single-Shot Readout of a Nuclear Spin Weakly Coupled to a Nitrogen-Vacancy Center at Room Temperature". *Physical Review Letters* 118:15, 2017, pp. 1–5. ISSN: 10797114. DOI: [10.1103/PhysRevLett.118.150504](https://doi.org/10.1103/PhysRevLett.118.150504). arXiv: [1612.07944](https://arxiv.org/abs/1612.07944).
22. R. Lo Nardo et al. "Spin relaxation and donor-acceptor recombination of Se⁺ in 28-silicon". *Physical Review B - Condensed Matter and Materials Physics* 92:16, 2015, pp. 1–6. ISSN: 1550235X. DOI: [10.1103/PhysRevB.92.165201](https://doi.org/10.1103/PhysRevB.92.165201). arXiv: [1503.05811](https://arxiv.org/abs/1503.05811).
23. S. Meiboom and D. Gill. "Modified spin-echo method for measuring nuclear relaxation times". *Review of Scientific Instruments* 29:8, 1958, pp. 688–691. ISSN: 00346748. DOI: [10.1063/1.1716296](https://doi.org/10.1063/1.1716296). arXiv: [arXiv:1011.1669v3](https://arxiv.org/abs/1011.1669v3).
24. J. J. L. Morton et al. "Nuclear relaxation effects in Davies ENDOR variants". *Journal of Magnetic Resonance* 191:2, 2008, pp. 315–321. ISSN: 10907807. DOI: [10.1016/j.jmr.2008.01.006](https://doi.org/10.1016/j.jmr.2008.01.006).

25. J. J. L. Morton et al. “Solid-state quantum memory using the ^{31}P nuclear spin”. *Nature* 455:7216, 2008, pp. 1085–1088. ISSN: 0028-0836. DOI: [10.1038/nature07295](https://doi.org/10.1038/nature07295). arXiv: [0803.2021](https://arxiv.org/abs/0803.2021).
26. R. L. Nardo. “Charge state manipulation of silicon-based donor spin qubits”. PhD thesis. 2015.
27. M. A. Nielsen and I. L. Chuang. *Quantum Computation and Quantum Information: 10th Anniversary Edition*. 10th. Cambridge University Press, New York, NY, USA, 2011. ISBN: 1107002176, 9781107002173.
28. T. O. Niinikoski et al. “Heat capacity of a silicon calorimeter at low temperatures measured by alpha-particles”. *Epl* 1:10, 1986, pp. 499–504. ISSN: 12864854. DOI: [10.1209/0295-5075/1/10/003](https://doi.org/10.1209/0295-5075/1/10/003).
29. J. O’Gorman et al. “A silicon-based surface code quantum computer”. *arXiv* 1:October 2015, 2014, pp. 1–11. ISSN: 2056-6387. DOI: [10.1038/npjqi.2015.19](https://doi.org/10.1038/npjqi.2015.19). arXiv: [1406.5149](https://arxiv.org/abs/1406.5149).
30. R. Orbach. “On the Theory of Spin-Lattice Relaxation in Paramagnetic Salts”. *Proceedings of the Physical Society* 77:4, 1961, pp. 821–826. ISSN: 0370-1328. DOI: [10.1088/0370-1328/77/4/301](https://doi.org/10.1088/0370-1328/77/4/301).
31. G. Pica et al. “Hyperfine Stark effect of shallow donors in silicon”. *Physical Review B - Condensed Matter and Materials Physics* 90:19, 2014, pp. 1–10. ISSN: 1550235X. DOI: [10.1103/PhysRevB.90.195204](https://doi.org/10.1103/PhysRevB.90.195204). arXiv: [1408.4375v1](https://arxiv.org/abs/1408.4375v1).
32. J. Preskill. “Reliable Quantum Computers”, 1997, pp. 1–24. ISSN: 1364-5021. DOI: [10.1098/rspa.1998.0167](https://doi.org/10.1098/rspa.1998.0167). arXiv: [9705031](https://arxiv.org/abs/9705031) [quant-ph]. URL: <http://arxiv.org/abs/quant-ph/9705031>. URL: <http://dx.doi.org/10.1098/rspa.1998.0167>.
33. M. Reagor et al. “Demonstration of Universal Parametric Entangling Gates on a Multi-Qubit Lattice”, 2017, pp. 1–7. arXiv: [1706.06570](https://arxiv.org/abs/1706.06570). URL: <http://arxiv.org/abs/1706.06570>.
34. M. P. Ross. “Bound exciton-assisted spin-to-charge conversion of donors in silicon”. PhD thesis. 2017.
35. A Schweiger and G Jeschke. *Principles of Pulse Electron Paramagnetic Resonance*. Oxford University Press, 2001. ISBN: 9780198506348. URL: <https://books.google.co.uk/books?id=tkvQQElkW1wC>.
36. N. Sclar. “Asymmetries in photoconductive properties of donor and acceptor impurities in silicon”. *Journal of Applied Physics* 55:8, 1984, pp. 2972–2976. ISSN: 00218979. DOI: [10.1063/1.333341](https://doi.org/10.1063/1.333341).
37. P. W. Shor. “Fault-tolerant quantum computation”, 1996. ISSN: 0272-5428. DOI: [10.1109/SFCS.1996.548464](https://doi.org/10.1109/SFCS.1996.548464). arXiv: [9605011](https://arxiv.org/abs/9605011) [quant-ph]. URL: <http://arxiv.org/abs/quant-ph/9605011>.

38. P. W. Shor. “Polynomial-Time Algorithms for Prime Factorization and Discrete Logarithms on a Quantum Computer *”. *SIAM Journal on Computing* 26:5, 1997, pp. 1484–1509. ISSN: 0097-5397. DOI: [10.1137/S0097539795293172](https://doi.org/10.1137/S0097539795293172). arXiv: [9508027](https://arxiv.org/abs/9508027) [quant-ph].
39. P. Shor. “Algorithms for quantum computation: discrete logarithms and factoring”. *Proceedings 35th Annual Symposium on Foundations of Computer Science*, 1994, pp. 124–134. ISSN: 0272-5428. DOI: [10.1109/SFCS.1994.365700](https://doi.org/10.1109/SFCS.1994.365700).
40. G. D. J. Smit et al. “Stark effect in shallow impurities in Si”. *Physical Review B - Condensed Matter and Materials Physics* 70:3, 2004, pp. 1–10. ISSN: 01631829. DOI: [10.1103/PhysRevB.70.035206](https://doi.org/10.1103/PhysRevB.70.035206). arXiv: [0310492](https://arxiv.org/abs/0310492) [cond-mat].
41. A. M. Tyryshkin et al. “Electron spin coherence exceeding seconds in high purity silicon”. *Nature Materials* 11:2, 2011, p. 18. ISSN: 1476-1122. DOI: [10.1038/nmat3182](https://doi.org/10.1038/nmat3182). arXiv: [1105.3772](https://arxiv.org/abs/1105.3772). URL: <http://arxiv.org/abs/1105.3772>.
42. G. S. Uhrig. “Exact results on dynamical decoupling by π pulses in quantum information processes”. *New Journal of Physics* 10, 2008. ISSN: 13672630. DOI: [10.1088/1367-2630/10/8/083024](https://doi.org/10.1088/1367-2630/10/8/083024). arXiv: [arXiv:0803.1427v2](https://arxiv.org/abs/0803.1427v2).
43. J. H. Van Vleck. “Paramagnetic relaxation times for titanium and chrome alum”. *Physical Review* 57:5, 1940, pp. 426–447. ISSN: 0031899X. DOI: [10.1103/PhysRev.57.426](https://doi.org/10.1103/PhysRev.57.426).
44. M. Vasmer and D. E. Browne. “Universal Quantum Computing with 3D Surface Codes”, 2018, pp. 1–21. arXiv: [1801.04255](https://arxiv.org/abs/1801.04255). URL: <http://arxiv.org/abs/1801.04255>.
45. Z. J. Wang and K. Zhang. “Dynamical suppression of nonlocal decoherence in two-state quantum systems”. *Communications in Theoretical Physics* 52:5, 2009, pp. 832–834. ISSN: 02536102. DOI: [10.1088/0253-6102/52/5/14](https://doi.org/10.1088/0253-6102/52/5/14). arXiv: [9803057](https://arxiv.org/abs/9803057) [quant-ph].
46. G. Wolfowicz. “Quantum Control of Donor Spins in Silicon and Their Environment”. PhD thesis. 2015.
47. G. Wolfowicz et al. “ ^{29}Si nuclear spins as a resource for donor spin qubits in silicon”. *New Journal of Physics* 18:2, 2016, p. 23021. ISSN: 13672630. DOI: [10.1088/1367-2630/18/2/023021](https://doi.org/10.1088/1367-2630/18/2/023021). arXiv: [1505.02057](https://arxiv.org/abs/1505.02057).
48. G. Wolfowicz et al. “Atomic clock transitions in silicon-based spin qubits.” *Nature nanotechnology* 8:8, 2013, pp. 561–4. ISSN: 1748-3395. DOI: [10.1038/nnano.2013.117](https://doi.org/10.1038/nnano.2013.117). arXiv: [1301.6567](https://arxiv.org/abs/1301.6567). URL: <http://www.ncbi.nlm.nih.gov/pubmed/23793304>.
49. G. Wolfowicz et al. “Conditional control of donor nuclear spins in silicon using stark shifts”. *Physical Review Letters* 113:15, 2014, pp. 1–5. ISSN: 10797114. DOI: [10.1103/PhysRevLett.113.157601](https://doi.org/10.1103/PhysRevLett.113.157601). arXiv: [arXiv:1405.7420v1](https://arxiv.org/abs/1405.7420v1).